

# Chapter 7

## Experimental Evidence for the Existence of Interfaces in Graphite and Their Relation to the Observed Metallic and Superconducting Behavior

Pablo D. Esquinazi and Yury V. Lysogorskiy

**Abstract** This chapter reviews the experimental evidence obtained for the existence of embedded interfaces between crystalline regions with Bernal and/or rhombohedral stacking order in usual graphite samples, and their relationship with the observed metallic and superconducting behavior.

### 7.1 Interfaces in Graphite Samples

Within the graphite literature there have been several publications on the lattice defects found in graphite structures, like point defects (vacancies and interstitials and their clusters), dislocations, twin boundaries, etc., see e.g. Chap. 3 in [1] and Refs. therein. For radiation defects the readers should refer to a recently published work [2]. The interfaces we are interested in this chapter are boundaries between either: (a) two slightly rotated crystalline regions around the  $c$ -axis, both with Bernal stacking order. It means the  $c$ -axes of the two regions are the same but their  $a$ -axes have a twist angle respect to each other, and (b) the boundaries between Bernal and rhombohedral stacking order regions. Both boundaries have been recognized time ago [3], but only recently their extraordinary properties have been partially studied, theoretically and experimentally.

---

P.D. Esquinazi (✉)

Division of Superconductivity and Magnetism, Institute for Experimental Physics II,  
University of Leipzig, Linnéstrasse 5, 04103 Leipzig, Germany  
e-mail: esquin@physik.uni-leipzig.de

Y.V. Lysogorskiy

Institute of Physics, Kazan Federal University, Kremlevskaya St. 18, 420008 Kazan, Russia  
e-mail: yura.lysogorskii@gmail.com

### 7.1.1 *Experimental Evidence Through Transmission and Scanning Electron Microscopy*

Kish graphite samples are obtained from iron and purified later with halogen gas at high temperatures. According to literature these kind of graphite samples show one of the largest resistivity ratio ( $R(300)/R(4.2)$ ) of nearly 50 [3] indicating a high degree of crystallinity. In p. 32 of the book of Inagaki [3] one finds an interesting double photo of the edges of a kish graphite sample, see Fig. 7.1 (left). As pointed out in that book, in those pictures one can see a regular stacking of layers at the edges of a Kish graphite sample. The difference in color are related to slightly different orientation, i.e. very probably rotations along a well aligned  $c$ -axis. The interfaces we are interested are those regions separating the single crystalline regions, each one characterized by a homogeneous gray color in Fig. 7.1 (left). The electrical transport “quality” of the Kish graphite samples can be derived from their large resistivity ratio, a ratio that depends very much on sample [3]. According to recent studies [4] the metalliclike behavior of graphite is not intrinsic but it comes from the interfaces properties, as will become clear in the next sections.

Regions with interfaces can be observed in nearly any well ordered graphite sample. Even in micrometer large graphite grains of ultrapure graphite powder, see

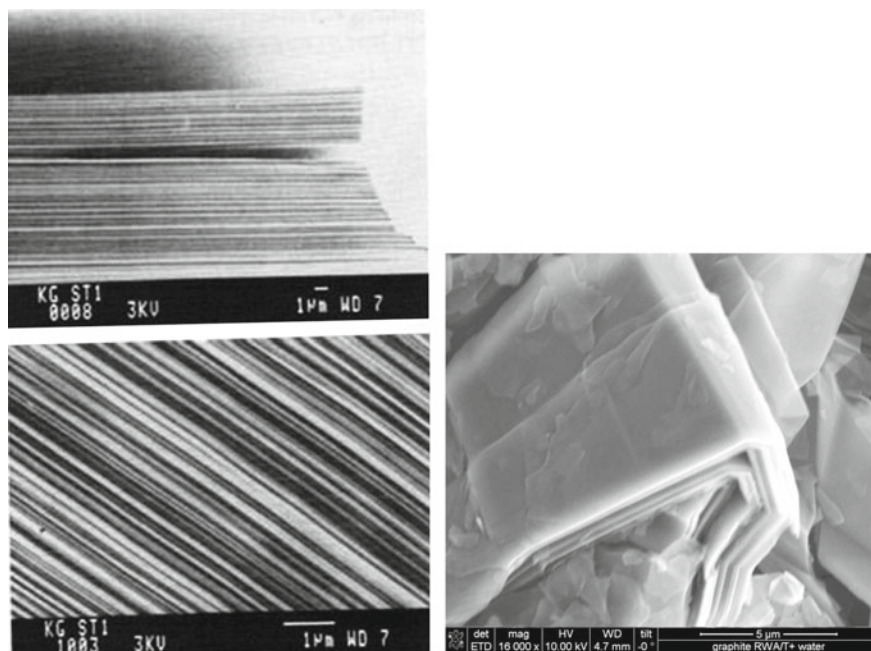


**Fig. 7.1** *Left* pictures are taken for a kish graphite sample from [3]. *Right* scanning electron microscope (SEM) picture is taken from [5] (see Supporting information in [5])

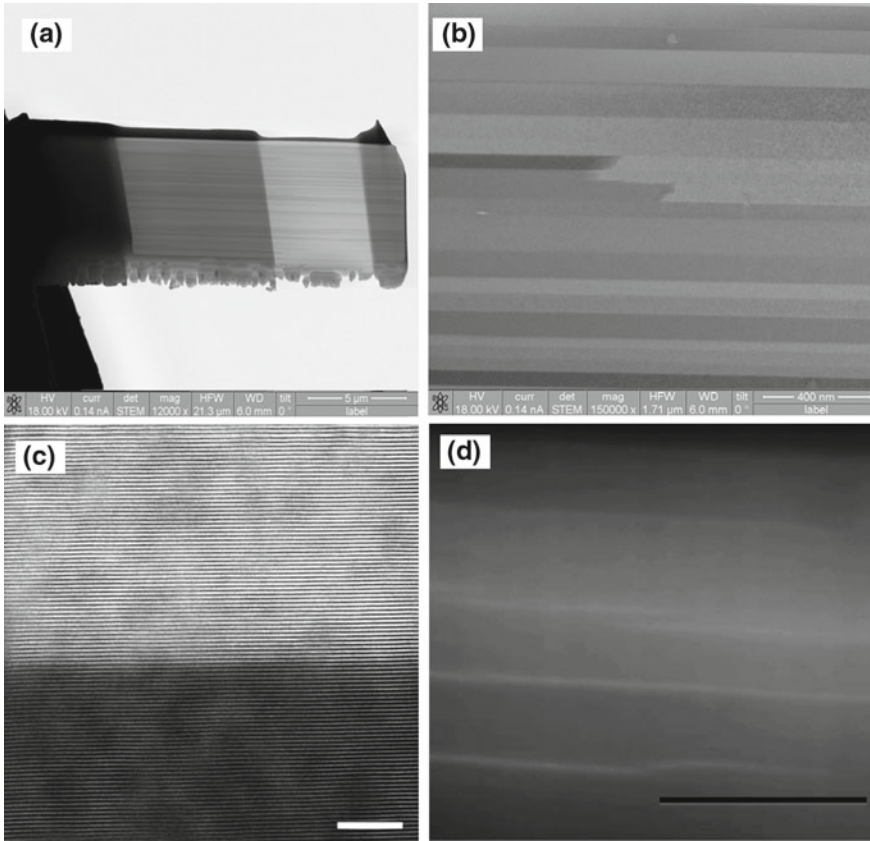


**Fig. 7.2** **a** SEM picture taken from a lamella of a HOPG sample after cutting, before leaving it on a substrate. The scale bar corresponds to 5  $\mu\text{m}$ . **b** Transmission electron microscope (TEM) picture of a HOPG ZYA sample, taken from [4]. The scale bar corresponds to 0.4  $\mu\text{m}$ . **c** TEM picture of a similar sample, taken from [6]. The scale bar corresponds to 5 nm. **d** TEM picture of a HOPG sample grade B, taken from [7]. The scale bar corresponds to 1  $\mu\text{m}$

Fig. 7.1 (right), those interfaces are evident [5]. If these interfaces have different electronic properties than the graphene layers of the single crystalline regions, several experimental methods like transport and magnetization may provide the response of those interfaces in parallel to the one from the graphene layers. If one does not take this possibility into account the interpretation of the experimental results can be misleading.

A much clearer picture of some details of the internal structure of graphite samples can be obtained using transmission electron microscopy (TEM) lamellae. In this case one takes TEM pictures with the electron beam pointing roughly parallel to the graphene planes and at relatively low energies (e.g.  $\sim 15$  keV). Figure 7.2a shows one SEM picture of a cut lamella (using a dual beam microscope) from a HOPG

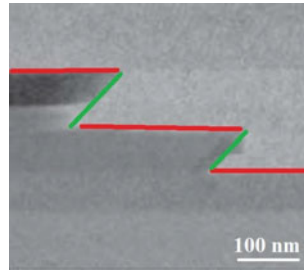


**Fig. 7.3** Transmission electron microscopy (TEM) picture of a highly oriented pyrolytic graphite (HOPG) ZYA sample taken parallel to graphene layers of the HOPG lamella. *Red lines* indicate the interfaces between twisted graphene blocks. *Green lines* shows the tilt grain boundaries. The scale bar indicates 100 nm. Image adapted from [4] (color figure online)

sample and fixed to a manipulator tip. In that picture and in spite of the relatively low resolution one can roughly observe single crystalline regions of graphite. These regions are more clearly observed using TEM, see Figs. 7.2b–d. Note the difference in the sharpness and the length of the interface regions between HOPG samples of grade A (b, c) and B (d). This difference plays an important role in the behavior of the magnetotransport and the size of the possible superconducting regions localized at the interfaces.

## 7.1.2 Twisted Layers: Moiré Patterns and Dislocation Lines

### 7.1.2.1 The Concept

One can divide the possible types of boundaries in graphite sample onto several groups: (a) two dimensional (2D) interfaces between twisted layers of graphene, which could be characterized by rotation angle  $\theta$  and lateral translation  $\delta$ . This type of interfaces produces the so-called moiré patterns [8, 9]; (b) 2D interfaces between regions with Bernal (ABA) and rhombohedral (ABCA) stacking and (c) one dimensional (1D) dislocation lines or topological line defects [10]. The location of some 2D and 1D boundaries are schematically shown in Fig. 7.3. However, the possible lattice defects in the graphite structure are much more plentiful. As example we refer to the exhaustive review of defects in graphite obtained after irradiation given in [2].

### 7.1.2.2 Moiré Patterns and Van Hove Singularities in Twisted Graphene Layers

In the work of Kuwabara and coauthors [8] the superperiodicity in scanning tunneling microscopy images of highly oriented pyrolytic graphite (HOPG) sample

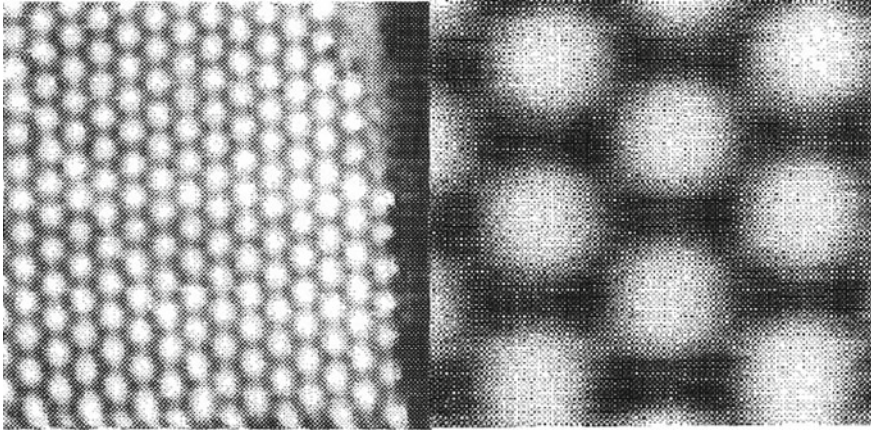


**Fig. 7.4** High-resolution scanning tunneling microscope (STM) at constant current images of a superperiodicity on a graphite (001) surface. Superperiodicity was associated with a moiré pattern, resulting from the overlap between a misoriented layer of graphite and the underlying graphite single crystal. The shown images are of size  $100\text{ nm} \times 100\text{ nm}$  (*left*) and  $22.5\text{ nm} \times 25.0\text{ nm}$  (*right*). The graphene lattice period itself is  $0.246\text{ nm}$  and is hardly visible on the given images. Adapted from [8]

was observed (see Fig. 7.4). This superperiodicity was associated with a moiré pattern (MP), resulting from the overlap between a misoriented layer of graphite and the underlying graphite single crystal. Moiré patterns on graphite consist of huge hexagonal lattices made of bright spots on STM images. It was proposed for the first time that in addition to the periodicity of the graphite lattice, the presence of a misoriented substrate a number of atomic spacings below the surface might be expected to introduce spatially periodic perturbations in the surface local density of states [8, 11].

In [12] the exhaustive analysis of different moiré patterns on graphene was done. Generally, one can classify the areas in misoriented graphene bilayer into three types: (a) normal, Bernal AB-stacking, (b) SlipAB-stacking and (c) AA-stacked graphene. In AA regions all carbon atoms of one layer are stacked over the carbon atoms of the other layer, whereas in AB regions only half of the atoms (Bernal stacking). SlipAB-stacking is obtained after a little shift of one layer in the AB-stacked structure.

DFT calculations of the density of states (DOS) at the Fermi level lead to the conclusion that only AB-stacked graphite regions are invisible, whereas AA-stacked graphite regions are the most visible, represented by bright spots. SlipAB-stacked graphite regions show an intermediate brightness in the STM images [12]. However, not all misorientation rotation angles between two adjacent layers will lead to a moiré pattern, but only under relative rotation angles between  $0^\circ$  and  $15^\circ$ , otherwise the regions with AA-stacking, which give the bright spots on STM images, disappear [12].

Further moiré patterns induced by rotations of surface and subsurface layers of graphite *bulk* samples were reported in [9, 13] (see Fig. 7.5). This evidence

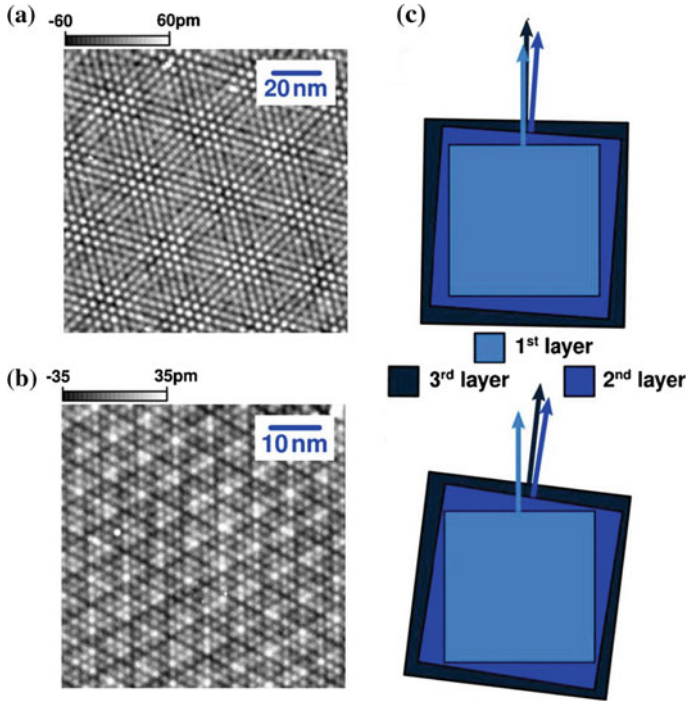


**Fig. 7.5** Scanning tunneling microscopy images of twisted graphene layers (a, b) along with its schematic of layer orientation (c). Moiré patterns could be formed by a misorientation of several graphene layers. Adapted from [13]

indicates that by the measurement of a transport property like the electrical resistivity or Hall effect one cannot be sure, which region of the sample provides the measured voltage signal. If the input current mainly flows through the interface regions where due to the rotation of the graphene blocks, a larger density of electrons than in ideal Bernal stacking order exists, then we will measure a voltage that can be due to the contribution of, at least, two resistances in parallel, as example see the discussion in Sect. 7.2.1. Although the anomalies in the DOS at the surface of usual graphite samples were reported already in 1990 [8], apparently their influence on the transport was not taken into account till 2008, where the authors observed that the absolute resistivity of graphite samples of different thickness, increased the smaller the thickness of the sample (see also a similar experiment in [14]) and that the metalliclike temperature dependence of bulk graphite turns to a semiconductinglike the thinner the graphite sample [4]. We note also that the authors in [15] after scanning the surface of a HOPG sample of high quality using Kelvin force microscopy (KFM) concluded on the coexistence of regions with “metalliclike” and “insulatinglike” behaviors showing large potential fluctuations of the order of 0.25 V. This micrometer large inhomogeneous domain distribution was not observed in disordered HOPG samples. Taking into account several reports on twisted graphene layers found on the

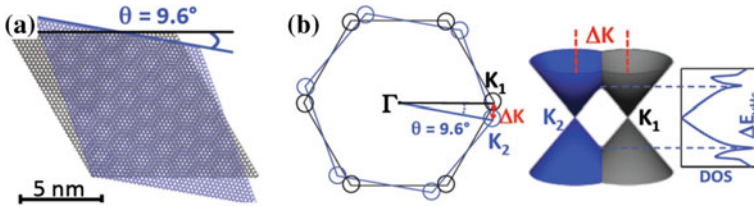


**Fig. 7.6** Illustration of a moiré pattern arising from the rotation of one graphene sheet relative to another by the twist angle  $\theta = 9.6^\circ$  (a) and mechanisms of emergence of Van Hove singularities as a consequence of this rotation (b). Dirac cones of each layer merge into two saddle points at energies  $\pm E_{\text{vHS}}$ . Adapted from [16]

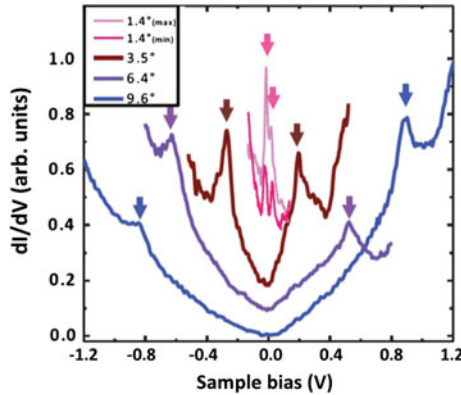


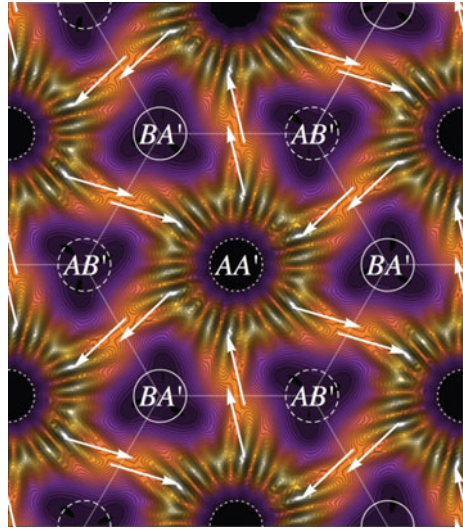
**Fig. 7.7** Scanning tunneling spectroscopy ( $dI/dV$ ) of the twisted graphene layers with different rotation angles  $\theta$ . Its intensity is proportional to local density of state of the sample, whereas the sample bias corresponds to shift with respect to the Fermi level. The energy difference between the Van Hove singularities (which are indicated by *arrows*) decreases with decreasing angle. Adapted from [16]

top surface of high quality graphite samples [8, 9, 13], it appears plausible that the results obtained using KFM [15] are related with the change in the electronic properties due to a inhomogeneous twist angle distribution of the top graphene planes in the samples.

In-depth systematic studies of moiré patterns and induced Van Hove singularities (vHs) in twisted graphene layers (TGL) was reported, for example, in [16] by means of scanning tunneling spectroscopy (STS) and *ab initio* simulations. The mechanism of increasing the local density of states is briefly described in Fig. 7.6. The rotation of graphene layers results in the equal rotation of its Brillouin zones by the same angle  $\theta$ . Thus, the Dirac cones of each layer are now centered in different points of the reciprocal space  $K_1$  and  $K_2$ . The cones merge into two saddle points at energies  $\pm E_{\text{vHS}}$  from the Dirac point, leading to vHs which generate peaks in the DOS [16]. The experimental evidence of this hypothesis is given in Fig. 7.7.

In addition, TGL under the interlayer bias could demonstrate very intriguing peculiarities such as the helical networks—the topologically protected electronic

**Fig. 7.8** Enhanced electron probability density (*bright areas*) between the regions with AA', AB' and BA' typical stacking of twisted bilayer graphene. In AA' regions all carbon atoms of one layer are stacked over the carbon atoms of the other layer, whereas in AB' or BA' regions—only the half of the atoms (Bernal stacking). A fully developed helical network state is formed. *White arrows* show the direction of the valley current. Adapted from [17]



states [17]. The emergence of this phenomenon could be explained in following manner: TGL forms moiré pattern which smoothly alternates between the three minimal types AA' (bright region on the STM image, see Fig. 7.4), AB' and BA' (dark region on the STM image). In AA' regions all carbon atoms of one layer are stacked over the carbon atoms of the other layer, whereas in AB' or BA' regions—only the half of the atoms (Bernal stacking). For any reasonable interlayer bias AA' bilayer is a good metal, whereas a band gap opens around each valley of TGL of Bernal-type stacking (AB' or BA'). Change of the topology of a tuned gap can be induced with a uniform bias  $U$  by smoothly transitioning from AB' to BA' stackings, which are related by mirror symmetry. Performing such an inversion between two adjacent regions in space gives rise to two topologically protected helical (TPH) modes per valley and spin. These modes could flow without resistance along the interface between the two regions [17]. On Fig. 7.8 a fully developed helical network state is shown. One can see the enhanced electron probability density between the regions with AA', AB' and BA' typical stacking. Electrons propagate without any dissipation along the links of the network. However, special types of defects, that could produce the valley scattering, can shut off the transmission through these links. The hydrogen adsorbates or vacancies were proposed as such defects [17]. Moreover, we note that the influence of  $H^+$  in between two graphene planes, on the dispersion relation of the carriers as well as on the DOS, is not thoroughly studied.

Besides the scanning tunneling spectroscopy, DOS of carbon structures could be also studied by means of resonance Raman spectroscopy. The Raman signal intensity increases significantly when both the incident and scattered photons are in resonance with transitions between vHs in the valence and conduction bands. In [18] the exhaustive study of the intensity of the G band peak in Raman spectra depending on the twist angle  $\theta$  in a range between  $0^\circ$  and  $30^\circ$  was performed (see Fig. 7.9).



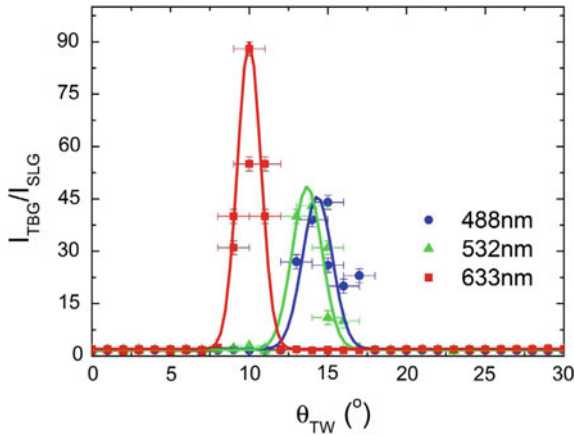


**Fig. 7.9** The ratio of Raman G peak intensity of twisted bilayer graphene to the intensity of single layer graphene ( $I_{\text{TBG}}/I_{\text{SLG}}$ ) for different samples with different twist angles  $\theta_{\text{TW}}$  between  $0^\circ$  and  $30^\circ$ . The Raman signal intensity increases significantly when both, the incident and scattered photons are in resonance with transitions between Van Hove singularities in the valence and conduction bands. *Blue, green, and red dots* are data taken at photon wavelengths equal to 488, 532 and 633 nm. Adapted from [18]

Among the TGL samples, only samples with twist angle from  $9^\circ$  to  $17^\circ$  demonstrate a strong increasing of the Raman intensity, whereas no enhancement was observed for TGL samples with low and high twist angles. So the experimental measurements as well as results of calculations by tight-binding method indicate that the vHs become more singular and intense for the case of the quasi-periodic moiré unit cell size of TGL since there are more  $k$  states at the flat region of the energy dispersion [18]. This fact may provide an answer to the observed interface size dependence of the Josephson critical behaviour [19], see Sect. 7.3.2.

One-dimensional topological defects in graphene embedded in a perfect graphene sheet are theoretically predicted and experimentally confirmed to have an almost flat band near Fermi energy and can act as a quasi-one-dimensional metallic wire [10, 20]. The results of STM/STS measurements of typical 1D topological defect on the surface of HOPG are shown in Fig. 7.10. As one can see, there are Van Hove-like singularities at Fermi level at the points along the 1D defect, whereas the singularity disappears far away from this defect [10]. Similar features were reported in [21]. Theoretical calculations by means of density functional theory (DFT) on the model system with periodic 1D defect line on graphene give similar results, i.e. presence of flat bands in band structure as well as vHs at the Fermi level (see Fig. 7.11). The flat band arise from the  $sp^2$  dangling bonds of undercoordinated carbon atoms at the edges of defects [10, 20].

As one can see, the flat bands in multilayer graphene structures could arise from moiré patterns as well as from 1D topological line defects. A discussion of the possible influence of vHs on the transport properties is given in Sect. 7.2.

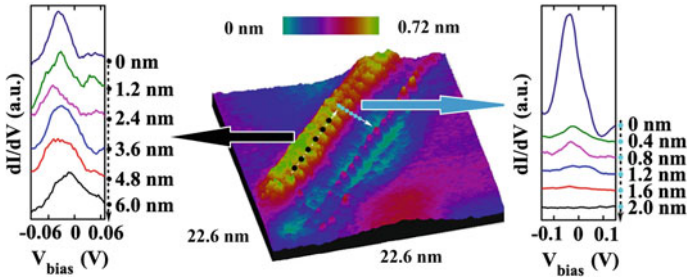


**Fig. 7.10** The  $22.6 \text{ nm} \times 22.6 \text{ nm}$  scanning tunneling microscopy image of an area with 1D defect on a HOPG surface (in the *center*) as well as the set of  $dI/dV$  spectra measured at different positions (*black and cyan dots* on the *left and right*).  $dI/dV$  is proportional to the local DOS of the sample, whereas the sample bias  $V_{\text{bias}}$  corresponds to shift with respect to Fermi level. Van Hove singularities at Fermi level are presented along the 1D defect, whereas the singularity disappears far away from this defect. Adapted from [10]

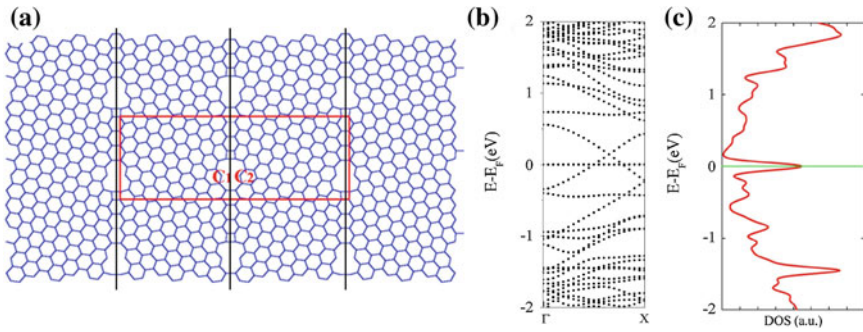


**Fig. 7.11** **a** The structure of particular 1D defect lines (*black line*) on a graphene sheet simulated by means of density functional theory, **b** its electronic band structure along the defect line and **c** the corresponding DOS. One can see the flat band in the band structure of given system as well as the Van Hove singularity at the Fermi level. Adapted from [10]

### 7.1.3 Recent Evidence for the Existence of Rhombohedral Stacking Order in Graphite

Because rhombohedral graphite (stacking order ABCA...) is expected to show flat bands at its surface, or at the interfaces with Bernal stacking order [22, 23], it is of interest to check whether this stacking order has been observed in graphite or multilayer graphene samples. The existence of this stacking order has been already pointed out in several publications in the past, see [24] and Refs. therein. Upon graphite sample, a concentration of up to 30% of this stacking order respect to the Bernal order appears possible, especially in natural graphite samples. According to [25], a certain amount of isolated rhombohedral crystallites has been detected in bulk samples without suffering severe shear deformation. In particular, it is interesting to

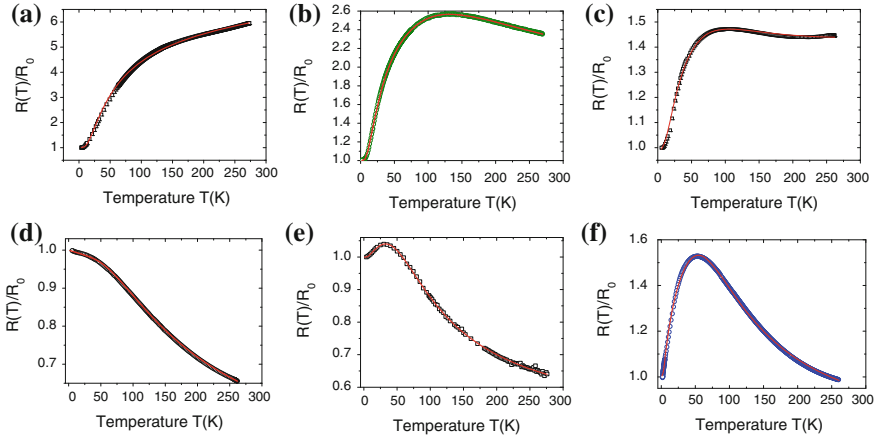


**Fig. 7.12** Normalized resistance  $R/R_0$  versus temperature for six HOPG samples with thickness, length (between voltage electrodes), width and  $R_0$ : **a**  $\simeq 20\ \mu\text{m}$ , 2 mm, 1 mm, 0.003  $\Omega$ ; **b**  $\simeq 10\ \mu\text{m}$ , 1 mm, 1 mm, 0.013  $\Omega$ ; **c**  $\simeq 50\ \text{nm}$ ,  $\sim 3\ \mu\text{m}$ ,  $\sim 3\ \mu\text{m}$ , 15  $\Omega$ . **d**  $\simeq 13\ \text{nm}$ , 14  $\mu\text{m}$ , 10  $\mu\text{m}$ , 490  $\Omega$ ; **e**  $\simeq 20\ \text{nm}$ , 5  $\mu\text{m}$ , 10  $\mu\text{m}$ , 32  $\Omega$ ; **f**  $\simeq 37\ \text{nm}$ , 27  $\mu\text{m}$ , 6  $\mu\text{m}$ , 69  $\Omega$ . The (red) lines through the experimental data are obtained from a parallel resistors model, see (7.1) and [30]. For similar experimental results and fits using both stacking orders, see [29]. Adapted from [30] (color figure online)

note the localization of an isolated rhombohedral graphite grain with thickness  $\sim 80$  and 550 nm length along the [0001] and [1100] directions. In another experimental work [26] the authors prepared multilayer graphene samples on freshly cleaved mica by exfoliation and studied them by scanning tunneling spectroscopy. The authors observed that multilayer graphene can exhibit a regular pattern of alternating ABA and ABC stacking with stacking areas as small as  $(200\ \text{nm})^2$ .

Evidence for the existence of flat bands near the Fermi level at the surface of epitaxially grown rhombohedral multilayer graphene has been recently reported [27]. The rhombohedral multilayers (sequences of about five layers and covering  $\sim 70\%$  of the sample total surface) were obtained by epitaxial growth on a 12  $\mu\text{m}$  thick 3C-SiC(111) film on a  $2^\circ$  off-axis 6H-SiC(0001). The existence of a flat band at the Fermi level has been concluded by scanning tunneling spectroscopy and angle-resolved photoemission spectroscopy. Further evidence for extended flat bands and gapped subbands for rhombohedral stacking was obtained by Raman spectroscopy in multilayers flake [28].

X-rays diffraction (XRD) can be used to check for the existence of the rhombohedral stacking in a graphite sample, if the amount of this phase and the size or thickness of these regions are large enough. We note, however, that there are several Bragg peaks in XRD, which are not suitable for distinguishing both stacking modifications of graphite. Both the  $(00l)$  and  $(hh0)$  peaks of the Bernal and rhombohedral stacking are superposed, for example. The easiest way to determine and approximately quantify the rhombohedral phase in a graphite sample is to restrict the  $2\Theta$  range between  $40^\circ$  and  $47^\circ$ . In this range one has two Bernal peaks at  $42.22^\circ$

(100) and  $44.39^\circ$  (101) and two peaks at  $43.45^\circ$  (101) and  $46.33^\circ$  (012) due to the rhombohedral stacking. Direct transport measurements from only the rhombohedral phase were not yet reported. However, recent transport studies in bulk and mesoscopic graphite samples with both stacking orders, indicate that the rhombohedral phase would behave semiconducting with an energy gap of the order of 100 meV and its interfaces with the Bernal phase metalliclike [29].

## 7.2 Experimental Evidence of the Contributions of Interfaces to the Transport Properties of Graphite Samples

### 7.2.1 *On the Intrinsic Temperature Dependence and Absolute Value of the Resistivity of Graphite*

Basically, the observed temperature dependence of the total resistance  $R(T)$  for all graphite samples shown in Fig. 7.12 and in the literature can be understood assuming the contribution of the graphene layers  $R_s(T)$  in parallel to that of interfaces  $R_i(T)$ :

$$R(T) = [R_s(T)^{-1} + R_i(T)^{-1}]^{-1}. \quad (7.1)$$

The fit curves in Fig. 7.12 were obtained assuming a semiconductinglike behavior for  $R_s(T)$  with a gap of the order of 30 meV, independently of the thickness of the sample, and an exponential thermally activated increase with activation energy of the order of  $\sim 50$  K [30]. The fits indicate that the graphene layers inside graphite behave semiconducting and that there is an extra metalliclike contribution which shows, however, an exponential increase with temperature, similar to that observed in granular superconductors [31]. The influence of this granular superconductivity in some internal interfaces of graphite samples is very probable the reason for the anomalous behavior of early high resolution magnetoresistance results of graphite flakes in [32]. We note that in case regions with rhombohedral stacking order embedded in the Bernal stacking order matrix would exist, it might be necessary to include a further resistance in parallel in (7.1), as has been done recently [29]. The parallel contribution of the rhombohedral stacking in the electrical resistance of a given graphite sample as well as a temperature dependent mobility appear to be necessary to include especially in samples that show minimum and maximum as a function of temperature, like in Fig. 7.12c. A systematic study of the temperature and thickness dependence of the resistance of more than 10 graphite samples with both stacking orders has been done recently [29]. This rhombohedral contribution, however, will be sample depend because the amount of this stacking relative to the Bernal stacking order depends on the graphite sample.

Note that the usual top contact electrodes configuration, or even a mixture of edge and upper graphene layer electrodes contacts in bulk samples involve always the

contribution of the  $c$ -axis resistivity. A contribution that in the simplest case and for fields normal to the graphene layers and interfaces, it does not change with applied field. However, the absolute value of this contribution is unpredictable because it depends on each sample. At least one of the free parameters used to fit the temperature dependent of the measured resistance, see Fig. 7.12, may depend on the  $c$ -axis resistance.

Because the contribution of the interfaces, internal as well as the two surfaces of a given graphite sample, cannot be easily subtracted from the measured total resistance, the absolute value of the resistivity in the  $a, b$  plane of the Bernal graphite structure remain unknown to some extent. If one plots the resistivity of graphite samples obtained from samples of the same batch but with different thicknesses, i.e. with similar density of interfaces as done in [4], this resistivity increases to values  $\rho_{a,b}(4\text{ K}) \gtrsim 200\ \mu\Omega\text{cm}$  for samples with the smallest interface contribution [29].

One may argue that the semiconductinglike dependence of the resistance for graphite samples with small enough thickness, see Fig. 7.12d, does not necessarily represent the intrinsic dependence because: (a) Either the lattice disorder in the thin graphite flakes is too large, or (b) ballistic and not diffusive transport may play a role. The hypothesis (a) can be easily ruled out through systematic Raman spectroscopy characterisation of the samples, see Sect. 7.2.2 for further references and details. Regarding the ballistic transport in graphite, indeed, a study of the mean free path with a parameter-free constriction method on bulk graphite HOPG samples indicates that the mean free path of the carriers in graphite is very large, i.e. several micrometers at low temperatures [33]. To check that the semiconductinglike behavior is intrinsic and not due to a hidden, non-diffusive carrier transport, we discuss here the results obtained using a relatively long graphite flake with low contribution of interfaces [34].

Figure 7.13 shows an optical microscope picture of a graphite sample of 20 nm thickness with 14 electrodes at different positions distributed through the whole 30  $\mu\text{m}$  sample length. The results of the resistance at different length of the same sample, see Fig. 7.13c, indicate that the absolute shift in resistance with length does not follow rigorously the Ohm law prediction due to an extra ballistic contribution. The data can be used to obtain the carrier mean free path versus temperature using Sharvin–Knudsen formula and Ohm’s law [34]. Especially the finite resistance one extrapolates at  $L \rightarrow 0$  from the experimental data of  $R(T, L)$  versus  $L$ , where  $L$  is the length between the voltages electrodes, can be used to obtain without free parameters the mean free path, see Fig. 7.13d. One main conclusion obtained in [34] is that the contribution of ballistic transport is relatively small for a sample with a length several times larger than the mean free path. Furthermore, the semiconductinglike behavior with a saturation at low temperatures is observed at all distances between the voltage electrodes indicating that this dependence is intrinsic and not related to the sample size. With the same parallel resistance model and the exponential temperature dependence appropriate for semiconductors, see Fig. 7.12, the obtained energy gap  $E_g \simeq k_B 350\text{ K}$  is independent of the distance between electrodes.

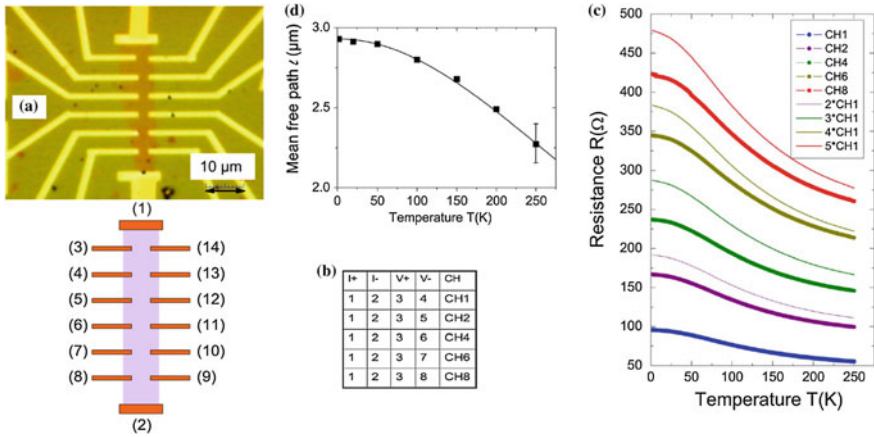


**Fig. 7.13** **a** Optical microscope photo of the measured graphite flake  $\approx 30 \mu\text{m}$  long,  $(5 \dots 8.5) \pm 0.3 \mu\text{m}$  wide and  $(20 \pm 2) \text{nm}$  thick with its 14 electrodes. **b** The *left sketch* shows the current and voltage electrodes configuration for the different channels. The *right picture* shows a table where the channels with the corresponding configuration for current and voltage electrodes are defined. **c** Temperature dependence of the resistance of the graphite flake at five different channels defined in **(b)**. The *continuous lines* represent the expected resistance if it would be just only proportional to the length between electrodes according to the Ohm law. **d** Temperature dependence of the carriers mean free path obtained from an equation assuming that the measured resistance has a ballistic, sample-length independent contribution and a Ohmic contribution, see [1–4] in [34]. The *continuous line* follows the equation  $\ell(T) = ((2.93)^{-1} + ((6.4 \times 10^5)/T^2)^{-1})^{-1}$  ( $T$  in K and  $\ell$  in  $\mu\text{m}$ ). After [34]

## 7.2.2 How Large Is the Carrier Density and Carrier Mobility in Ideal Graphite? Quantum Oscillations in the Transport Properties Revised

Figure 7.14 shows the field dependence of the Hall coefficient for graphite flakes of different thickness obtained from kish graphite samples [35, 36]. In those results there are several interesting details we would like to emphasize:

(A) The amplitude of the Shubnikov-de Haas (SdH) oscillations tends to decrease the smaller the thickness of the sample. This tendency appears more systematic in Fig. 7.14b. If the crystalline quality between the samples remains similar, this result points out that these oscillations are not intrinsic. A graphite sample with a thickness of 18 nm (and several tens of square microns area) can certainly be considered as bulk, if homogeneous.

One may argue that the reason for the decrease of the amplitude of the SdH oscillations is the decrease in the amount of perfect graphene layers, in other words the increase in the lattice disorder existing in the sample. Within this hypothesis small patches of ideal graphene layers coexist with disordered graphene layers and the SdH occur only in the ideal graphene layers. However, the experimental evidence obtained

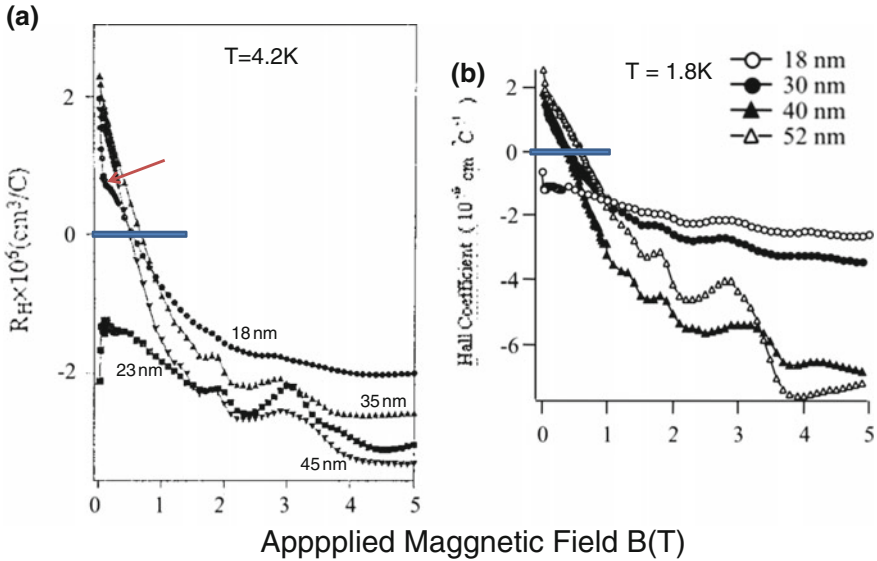


**Fig. 7.14** **a** Hall coefficient as a function of applied field normal to the graphene planes of graphite flakes of different thickness taken from a kish graphite sample. The red arrow points to the field region where a clear kink shows in the field dependence of the 18 nm thick sample. Adapted from [35]. **b** Similar but from other kish sample. Adapted from [36]. The blue horizontal bars shows the zero coefficient value. With exception of the 23 nm thick sample in (a) and the 18 nm in (b), all other samples show a clear change in sign of the Hall coefficient from positive to negative increasing field. This sign change occurs at a sample-dependent field (color figure online)

by different studies the last years indicates that this hypothesis is not always correct. For example: (a) There is no evidence from Raman that the thinner the sample the larger the disorder, see e.g. [4, 29, 37], as example. (b) The amplitude of the SdH oscillations depends on the region one measures within the same sample, as Fig. 7.15 shows [38]. This result indicates that there is a non-homogeneous distribution of patches where the density of carriers is large enough to provide SdH oscillations with a similar period (in  $1/B$ ) to that observed for bulk graphite samples. The question is then whether those regions, where SdH oscillations occur, are perfect graphene layers or the opposite, regions where the lattice disorder or the interface regions with their higher DOS (see Sect. 7.1.2), are those with enough carrier density.

A partial answer to this question was given by the authors in [38] after irradiating with  $\text{Ga}^+$  ions only a part of the graphite flake, see Fig. 7.15. The irradiated fluence introduced an average defects (e.g. vacancies) concentration of  $\sim 10^{12} \text{cm}^{-2}$ . We see that after irradiation the amplitude of the SdH oscillations, measured only in that part of the sample, increased drastically and started to be measurable at lower magnetic fields, see Fig. 7.15a. From the period in  $1/B$  one can estimate a carrier concentration per graphene layer  $n \sim 3 \times 10^{11} \text{cm}^{-2}$  similar to that found in bulk HOPG samples in literature [24, 39]. Note that the SdH oscillations in the small graphite flake as

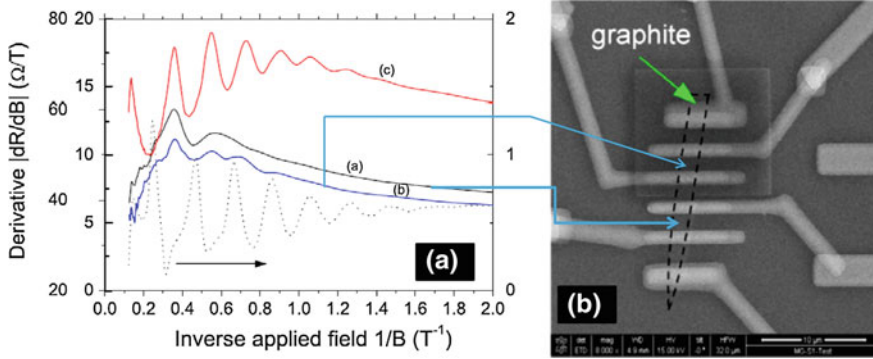


**Fig. 7.15** **a** First derivative of the magnetoresistance at  $T = 4$  K of different graphite samples. Curves (a) and (b) ( $0 - 20 \text{ } \Omega/\text{T}$  range) represents the results obtained from two different parts (follow *blue arrows*) of the same graphite flake shown in the picture in **(b)**. The curve (c) ( $20 - 80 \text{ } \Omega/\text{T}$  range) represents the results obtained from the same part **(a)** of that flake but after irradiation with  $\text{Ga}^+$  ions with a fluence of  $5 \times 10^{11} \text{ Ga}^+/\text{cm}^2$ . The *dashed line* (right y-axis) was obtained for the bulk HOPG sample of size  $2 \times 1 \times 0.2 \text{ mm}^3$ . Adapted from [41]. **b** Scanning electron microscope image of a 15 nm thick graphite flake (*dashed line* denotes its borders) with six Au/Pt electrodes (scale bar denotes  $10 \text{ } \mu\text{m}$ ). One recognizes the region with 300 nm thick negative electron beam resist used to protect part of the graphite flake from the  $\text{Ga}^+$  irradiation. Adapted from [38] (color figure online)

well as after  $\text{Ga}^+$  irradiation are shifted respect to that obtained for the bulk HOPG samples, see Fig. 7.15a. From this result we would conclude that the origin for the SdH oscillations in graphite is not related to perfect, defect-free graphene layers but the opposite.

It is interesting to note that after a similar second  $\text{Ga}^+$  irradiation on the same part of the graphite sample shown in Fig. 7.15, the absolute value of the magnetoresistance (MR) and the resistance itself changed as expected, i.e. the resistance increased and the MR decreased [38]. Nevertheless, the SdH oscillations did not change qualitatively, i.e. these start to be measurable at a similar low field and with a similar oscillation period (in  $1/B$ ). This result indicates that no further increase in the carrier density has been achieved when the distance between the produced defects (e.g. vacancies) on each graphene layer is below 2 nm. Apparently, this result is related to the  $\sim 3 \text{ nm}$  range where a modification of the electronic structure due to a single vacancy has been measured [40].

A possible reason for the observation of the SdH oscillations in the virgin thin sample at high fields only, can be as follows [41]: For the measured sample area that gives curve (a) in Fig. 7.15 there are no SdH oscillations up to a field  $B \simeq 1.8 \text{ T}$  in clear contrast to the irradiated sample. This fact can be understood assuming that in most of this sample part  $n_0 \lesssim 10^9 \text{ cm}^{-2}$ . Then, the corresponding Fermi wavelength  $\lambda_F \gtrsim 0.8 \text{ } \mu\text{m}$  is of the order of the sample size and larger than the cyclotron radius  $r_c = m^* v_F / eB$  for  $B > 0.07 \text{ T}$  assuming  $m^* = 0.01m$  ( $m$  is the free electron mass). In this case we do not expect to observe any SdH oscillations. However, for  $B \simeq 1.8$



and 2.8 T two maxima are observed. From the measured “period” in  $1/B$  as well as from the first field at which the first maximum appears we estimate the existence of domains of size  $< 2r_c \lesssim 100$  nm at which  $\lambda_F \lesssim 50$  nm, i.e. domains with  $n_0 \gtrsim 10^{11}$  cm $^{-2}$  within a matrix of much lower carrier concentration. This indicates that the description of the SdH oscillations in real graphite samples can be achieved only within the framework of inhomogeneous 2D systems [42, 43]. At the end of this section we discuss experimental studies that provide carrier concentrations  $n_0 \lesssim 10^9$  cm $^{-2}$  for ideal graphene layers inside graphite, supporting the hypothesis that the usually measured SdH and de Haas-van Alphen (dHvH) oscillations in bulk graphite samples in literature, from where carrier densities  $n \gtrsim 10^{11}$  cm $^{-2}$  are extracted, do not represent ideal graphite.

(B) From the SdH oscillations period the authors in [35, 36] obtained that the cross section of the Fermi surface in the thin graphite flakes appears to be half of the one for bulk graphite samples, implying that the flakes should have a smaller carrier density by the same amount. Taking into account the large density of interfaces in kish graphite samples, see Fig. 7.1, one can speculate that the reduction of the SdH oscillations is related to a smaller amount of interfaces in thinner samples, assuming that the interfaces have a larger density of carriers than the graphene planes.

(C) For most of the samples shown in Fig. 7.14 there is a clear change of sign of the Hall coefficient, from positive to negative, increasing magnetic field. In particular in the 18 nm flake in Fig. 7.14a we see a clear kink in the field dependence. The field at which there is a crossover from positive to negative, depends on the sample, suggesting a non-intrinsic nature. A recent study of the Hall coefficient measured in different graphite samples since 1955 and in graphite flakes without interfaces, indicates that the negative sign is not intrinsic of the ideal graphite [44], as we discuss below in Sect. 7.2.3.

Finally, the reported values for the Hall coefficient in Fig. 7.14 [35, 36] are five orders of magnitude smaller than the one reported in the literature [44] (see Sect. 7.2.3); this large discrepancy might be due to an error in the units or a missing factor in the calculation of the Hall coefficient in [35, 36].

### 7.2.2.1 An Experimental Approach to Obtain the Intrinsic Carrier Density and Mobility

The measurement of the carrier mean-free path  $\ell$  is not straightforward and, in general, the value obtained depends on several other not well-known parameters within the selected transport model, usually based on a Drude–Boltzmann approach. However, in case of ballistic conduction, there are at least two more transparent methods to obtain  $\ell(T)$  without adjustable parameters. One method is to measure the resistance as a function of the sample length as has been done in [34] and the results shown in Fig. 7.13c can be used to obtain  $\ell(T)$ , as shown in Fig. 7.13d. The other method is based on the measurement of the longitudinal resistance as a function of the constriction width  $W$ , a constriction located between the voltage electrodes, see Fig. 7.16a, b. The resistance can be quantitatively understood taking into account

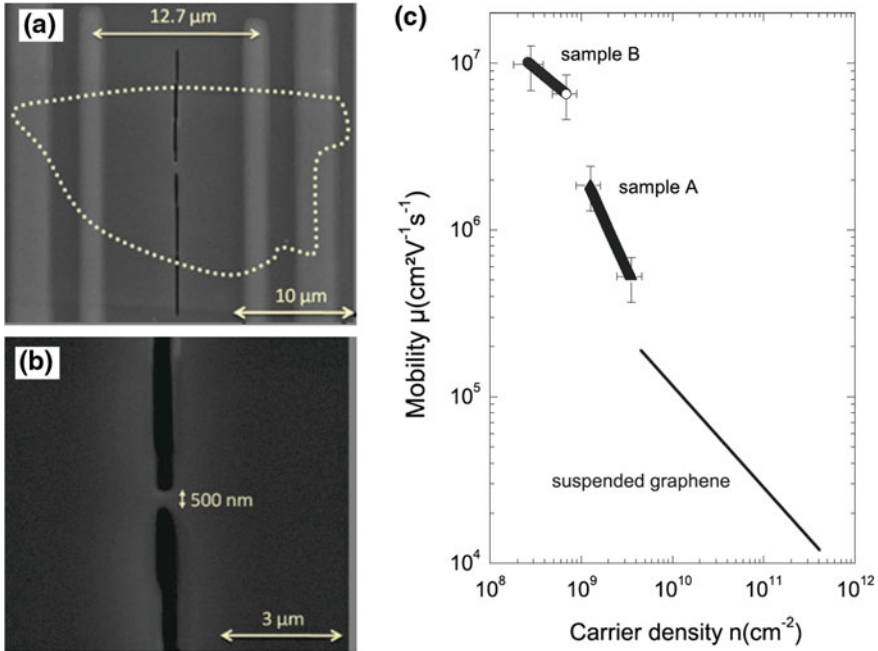


**Fig. 7.16** **a** Graphite flake (sample A of 15 nm thickness, the *point line* denotes the edge of the sample) with four electrodes and a constriction in the *middle*. **b** Blow out of a constriction of 500 nm size in sample A. **c** Mobility versus carrier density obtained from the measurements of the resistance at different constrictions widths and at different temperatures. The points are obtained between 300 and 10 K for sample B of 40 nm thickness (60 K for sample A). The *line* corresponds to the data of a suspended graphene sample at 20 K from [45]. Taken from [46]

three contributions, the ballistic one given by the Knudsen–Sharvin resistance [33]; a logarithmic term due to the ohmic, spreading resistance in two dimensions, and a third term due to the ohmic resistance of the constriction itself [46]. The resistance is expected to show an oscillatory behavior as a function of  $W$  or the Fermi wavelength  $\lambda_F$  [47, 48], as observed experimentally in bismuth (Bi) nanowires [49] as well as in GaAs devices [50, 51]. Although the experiments were done changing only five times the constriction width of the sample, the behavior obtained appears compatible with the one observed previously allowing to calculate the mean free path  $\ell(T)$ , the Fermi wavelength  $\lambda_F(T)$  and the mobility  $\mu(T) = (e/h)\ell(T)\lambda_F(T)$ . The carrier density per graphene layer can be calculated from  $n = 2\pi/\lambda_F^2$ .

The results for the mobility versus carrier density per graphene layer of the measured samples are shown in Fig. 7.16c and indicate that the intrinsic carrier density (without the contribution of the interfaces) is three orders of magnitude smaller than the one obtained in literature for bulk graphite samples with interfaces, i.e.  $n(T < 10\text{K}) \lesssim 10^9 \text{ cm}^{-2}$  per graphene layer [33, 46]. From the results in bulk HOPG and thin flakes one obtains that the mean free path  $\ell(T) \propto T^{-2}$  reaching values of

microns at room temperature [33, 34, 46]. Such large mean free path and small carrier density (large Fermi wavelength) indicate that the carrier mobility should be large. Indeed the obtained carrier mobility is two orders of magnitude larger than the one found in literature obtained from graphite samples with interfaces.

There is further experimental evidence that indicates that the carriers mean free path is extraordinarily large. The reported clear increase of the (basal) magnetoresistance (for magnetic fields normal to the graphene planes) with sample size in, for example, bulk graphite samples (see Fig. 2 in [52]), graphite thin flakes (see Fig. 10 in [4]) and graphite thin flakes with constrictions (see Fig. 6 in [46]) demonstrates that the carrier mean free path is several micrometers long. The decrease of the mean free path with temperature, see e.g. Fig. 7.13d, is the main reason for the *increase* of the magnetoresistance with temperature observed in relatively small graphite samples, see Fig. 6 in [4], or graphite samples with constrictions, see Fig. 11 in [4]. The magnetoresistance of small graphite samples can increase or decrease with temperature upon the relative size of the carriers mean free path to the effective (lateral) sample size.

We note that several interpretations of the experimental transport data of real graphite samples relied on the assumption that these were intrinsic properties. As an example, the carrier (electron plus hole) densities obtained from the SdH oscillations, see above in this section, are several orders of magnitude larger than the one the graphene planes have in graphite, see e.g. Fig. 7.16. For example, at low temperatures, the carrier density per graphene layer in graphite assumed in the literature is  $n_0 > 10^{10} \text{ cm}^{-2}$ , as one can read in the standard book of Kelly [24], or the old publication from [53], or from recently published work [54] ( $n_0 \simeq 10^{12} \text{ cm}^{-2}$ ) or [55] ( $n_0 \simeq 2.4 \times 10^{11} \text{ cm}^{-2}$ ).

Therefore, it is interesting to reconsider the development of the electronic band structure of graphite, which came out based on experimental parameters of the last, say, 80 years. As pointed out in previous publications [41, 56] we would like here to note the following development:

- Hund and Mrowka from Leipzig published one of the first calculations of the energy band structure of simple atom lattice structures, in particular of diamond [57], also published by Kimball in the same year [58]. The first attempt to calculate the dispersion relation of the graphite structure was also published by Hund and Mrowka from Leipzig in the same year [59]. In this last publication, the authors analyzed the energy states of the graphene structure and wrote explicitly the dispersion relation for this structure assuming  $s$ -wave functions, a dispersion relation that partially resembles the one we use for graphene within the tight binding approximation.
- Two-dimensional calculations assuming a coupling  $\gamma_0$  between nearest in-plane neighbors C-atoms on the graphene plane of zero-gap semiconducting graphite gave a carrier density (free electrons and positive holes per C-atom)  $n(T) \simeq 0.3(k_B T / \gamma_0)^2$  [60]. If one assumes  $\gamma_0 \simeq 3 \text{ eV}$  the effective carrier density per C-atom at 300K would be  $n(300) \simeq 2 \times 10^{-5}$ . This is equivalent to  $7.64 \times 10^{10} \text{ cm}^{-2}$  total carrier density at 300K using the areal density of carbon atom per

graphene layer ( $=3.82 \times 10^{15} \text{ cm}^{-2}$ ). A similar value for the total carrier density was obtained for bulk HOPG samples at similar temperatures using the constriction method [33]. Moreover, the obtained temperature dependence carrier density can be fitted up to  $\sim 200 \text{ K}$  by  $n[\text{cm}^{-2}] \simeq n_0 + 10^5 T^2 + 7.5 \times 10^3 T^3$  with  $T$  in [K] and  $n_0 \simeq 2 \times 10^8 \text{ cm}^{-2}$ . We note, however, that the same data can be also well explained by a semiconducting-like exponential function  $\exp(-E_g/2T)$  with an energy gap  $E_g \sim 50 \text{ meV}$ .

- Because several experimental values obtained from bulk graphite samples with interfaces indicated a finite  $n(T \rightarrow 0) = n_0 > 0$  then more free parameters in the tight-binding electronic band structure calculations were included in order to provide a finite carrier density at zero temperature. For example, with a new coupling  $\gamma_1$  between C-atoms of type  $\alpha$  in adjacent planes one obtains  $n(T) = a(\gamma_1/\gamma_0^2)T + b(T/\gamma_0)^2 + c(T^3/\gamma_0^2\gamma_1) + \dots$  ( $a, b, c, \dots$  are numerical constants), where the “accepted” value for  $\gamma_1 \sim 0.3 \text{ eV}$ . Also in this case  $n(T \rightarrow 0) \rightarrow 0$ . To fit experimental data and obtain a finite Fermi energy  $E_F$ —in the simplest case  $E_F \sim \gamma_2$  [24, 61]—up to seven free parameters were and still are introduced, even for carrier density as small as  $n \simeq |-8 \times 10^9| \text{ cm}^{-2}$  ( $E_F \simeq -29 \text{ meV}$ ) [62].

Taking into account the exhaustive experience accumulated in gapless or narrow gap semiconductors [63] we should actually expect that at least part of the measured carrier density at low temperatures is not intrinsic of the graphite structure but it is influenced by interfaces, impurities and/or defects in the graphite/graphene lattice. We note that a carrier density of the order of  $10^8 \text{ cm}^{-2}$  means one carrier in  $1 \mu\text{m}^2$  graphene area, which could be produced actually by having a single vacancy or impurity in the same graphene area, in case one carrier is generated by one of these defects [41, 64]. Therefore, we should cast doubts on the relevance of related electronic band structure parameters obtained in the past.

### 7.2.3 On the Intrinsic Low-Field Hall Coefficient of Graphite

Recently reported study of the low-field Hall coefficient of thin graphite flakes and a overall comparison with literature arrived to the conclusion that its negative sign is not intrinsic but it is due to the contribution of the internal interfaces. The temperature dependence of low-field  $R_H$  shown in Fig. 7.17 for three different graphite flakes obtained from a HOPG sample and its behavior at higher fields (sample S3 in the figure) suggests that the change of sign is not intrinsic but it is due to the contribution of interfaces [44]. From the temperature dependence of the resistance one can roughly guess how important is the contribution of the interfaces for the transport properties of given sample. The samples in Fig. 7.17 showed different interface contributions, being the sample S1 with smaller contribution that in samples S2 and S3 [44].

The available data would indicate also that the reported behavior, specially the change in sign of the Hall coefficient as a function of field in Fig. 7.14 [35, 36], is not intrinsic but due the contribution of interfaces. If these interfaces would have

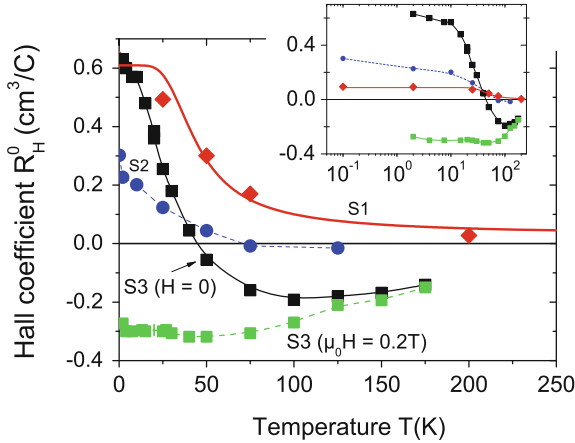


**Fig. 7.17** Temperature dependence of the low-field Hall coefficient for the three studied samples. For sample S3 (*black squares*) we show also the Hall coefficient (*green squares*) obtained at a field  $\mu_0 H = 0.2\text{ T}$  applied normal to the interfaces. The data from sample S1 in the main panel of the figure were multiplied by a constant factor of 6.7. The *inset* shows the same data but in a logarithmic temperature scale. The line through the S1 data points follows the function  $R_H^0 = (11^{-1} + (4 \times 10^{-3} \exp(300/(2T)))^{-1})^{-1}$ . All other lines are only a guide to the eye. Taken from [44]

superconducting properties we expect a finite, negative contribution at high enough temperatures, as can be seen for samples S2 and S3 in Fig. 7.17, similarly at high enough applied fields [44], see also Fig. 7.14. At low temperatures and at low enough applied fields, we expect that the contribution of the interfaces, if they exist in a given sample, to the Hall signal will be minimum. From old and new available Hall data [44] we can conclude that the intrinsic, low magnetic field Hall coefficient of graphite appears to be positive with a low-temperature value around  $0.1\text{ cm}^3/\text{C}$  and a temperature dependence that follows closely that of a semiconductor with an energy gap of the order of  $300 \dots 400\text{ K}$ , in agreement with the fits of the longitudinal resistance of different samples, see Fig. 7.12 [30].

### 7.2.4 Trying to Get the Response of a Single Interface

It is clear that one cannot obtain the transport behavior of an interface of a graphite sample directly, because one cannot introduce simply electrical contacts inside the sample without destroying it. The use of electrical contacts at the edges of the interfaces will be described in the next section. Therefore, a simple way to obtain a rough signal of a single interface is to localize voltage electrodes at two sides of a step of a graphite flake, see the left picture in Fig. 7.18. The graphite flake measured in [65] was heterogeneously thick and several micrometers long, allowing to find regions to locate voltage electrodes that may pick up more clearly the response of a single interface.

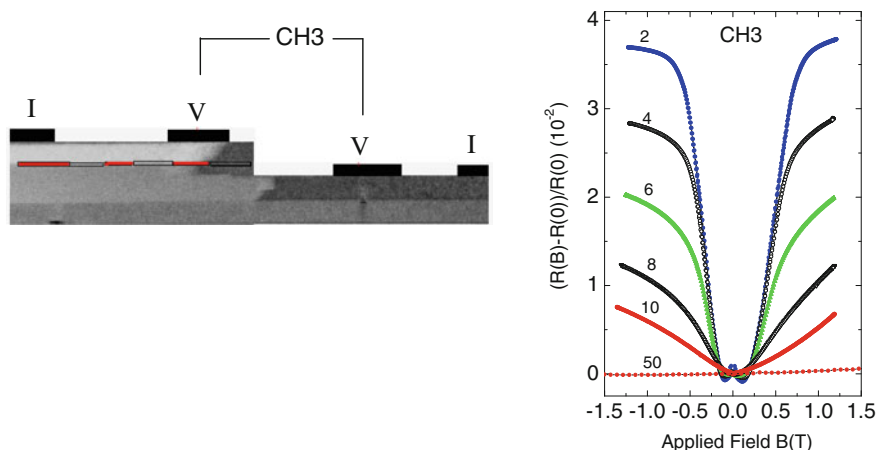


**Fig. 7.18** The *left picture* shows an electron transmission microscope picture of a 200 nm thick lamella with the  $c$ -axis of the graphite structure running normal to the interfaces between the crystalline graphite structure. The thickness of the single crystalline regions (defined by the homogeneous gray color regions) is  $\sim 70$  nm. At the top of the TEM picture the positions of the electrodes of channel 3 (CH3) and current ( $I$ ) electrodes are schematically drawn. In case superconducting regions exist between the CH3 electrodes we expect to see some evidence in the voltage drop. The *right figure* shows the magnetoresistance measured at CH3 versus magnetic field applied parallel to the graphene planes within  $\pm 3^\circ$  at different temperatures. Adapted from [65] (color figure online)

The magnetoresistance of a region of the selected sample with voltage electrodes at the up and low sides of a 120 nm large step height is shown in the right picture of Fig. 7.18. The magnetoresistance measured at this location of the sample shows an unique behavior that suggests the existence of inhomogeneous or granular superconductivity in that sample region. At low  $T$  the magnetoresistance increases abruptly at  $B \gtrsim 0.25$  T and saturates at  $B \gtrsim 0.75$  T, see Fig. 7.18. We note that in order to decrease substantially the large background of the intrinsic magnetoresistance of graphite observed for fields parallel to the  $c$ -axis, the magnetic field in that experiment [65] was applied nearly parallel to the graphene planes and interfaces, reducing in this case the field component normal to the graphene layers [66]. The small negative magnetoresistance obtained at low fields is probably related to the magnetic order due to defects (DIM, see Chaps. 1–3) that exists in parts of the selected sample, as shown in more detail in [65].

### 7.3 Experiments with TEM Lamellae

A direct measurement of the transport properties of the interfaces is not a simple task. Even if one would prepare a graphene bilayer with a selected twist angle between the two graphene planes, locating the contact at the top of the graphene plane does not

provide the response of an internal interface. The idea used in recent publications [7, 19, 56, 67] was to prepare TEM lamellae from the bulk graphite sample in question and deposit electric contacts at the edges of the lamella. In this case one gets a better chance to measure the direct voltage response of several interfaces in parallel when an electrical current is passing through. If some of those interfaces show superconducting properties, then it is clear that a negligible voltage should be measured. A graphite TEM lamella is in general prepared using the in-situ lift out method of a dual beam microscope (FIB/SEM). The TEM lamellae are cut perpendicular to the graphene layers and to the embedded interfaces using the  $\text{Ga}^+$  ion source. Before cutting it, a thin film is deposited using electron beam induced deposition (EBID) in order to protect the internal structure of the sample from the  $\text{Ga}^+$  ions used to cut the lamella. Nevertheless, a region  $\sim 20$  nm thick at each of the edges of the lamellae is contaminated with Ga. This region remains highly disordered and high electrical resistance [38]. The usual four contacts method used to measure the voltage response of the lamella prevents therefore the contribution of this  $\sim 20$  nm thick disordered layer in the measurement [68]. The total procedure to obtain a thin TEM lamella with low Ga contamination and well polished edges (like the several steps milling of the main surface done at progressively high to low currents) requires however large experience with several non-simple preparation details and the use of the technical capabilities of the dual beam microscope [68]. Lamellae with different thickness  $100 \text{ nm} \lesssim d \lesssim 1 \text{ }\mu\text{m}$  were prepared and contacted, see Fig. 7.19. The electron transmission diffraction pattern obtained with the beam parallel to the graphene layers provides information on the crystalline regions and their defective parts parallel to the graphene layers, as shown in Figs. 7.2 and 7.19.

In this introductory section we show experimental results of different graphite lamellae published recently and discuss several open issues on these results. We divide the presentation into three parts, namely, (A) the temperature dependence of the voltage (or resistance) at different constant currents, (B) Voltage-Current ( $I-V$ ) characteristics at different temperatures and (C) field dependence. The other two subsections handle on the size dependence of the critical behavior (Sect. 7.3.2) and the results obtained from a graphite sample of lower grade (Sect. 7.3.1).

#### (A) Temperature Dependence at Constant Currents

Figure 7.20 shows the results from three different lamellae, two of them (a, b) with the usual contacts configuration in series (like in Fig. 7.19) and one (c) with a Van der Pauw configuration, i.e. the contacts were positioned at the edges of the lamella [67, 68]. The measured resistance is in all cases non-ohmic, i.e. its absolute value and behavior with temperature depends on the input current. We note that the absolute value of the resistance can be relatively large, up to  $10^6 \text{ }\Omega$ , at high enough temperature, where the input current does not influence notably. In case of the lamella in Fig. 7.20a the obvious transition shifts to lower temperatures or vanishes increasing the input current. Something similar is observed in the lamella in (b) below 20 K for input currents  $I \leq 10 \text{ nA}$ . The noise level observed in that measurement ( $\sim 300 \text{ nV}$ ) is related to the intrinsic properties of the sample and not to the electronic equipment. It was interpreted as due to the contribution of different Josephson coupled

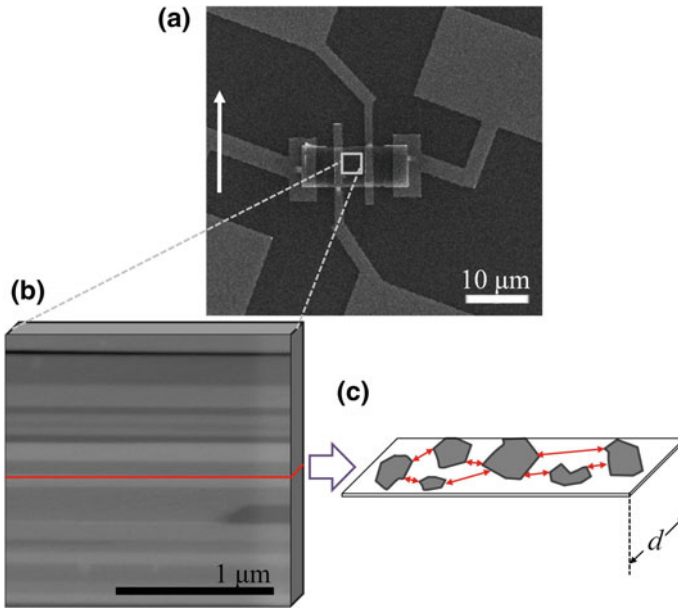


**Fig. 7.19** **a** Scanning electron microscope picture of a lamella on a Si/Si substrate with its four in series contact arrangement. **b** Transmission electron microscope picture of the internal microstructure of a lamella from the same batch. The *red line* is a guide to indicate the possible existence of an interface between two crystalline regions with a given twisted angle around the  $c$ -axis. **c** The model behind the observations is that localized regions exist within certain interfaces in which superconducting patches exist (*grey regions* in the sketch) Josephson coupled (*red lines* connecting them). The size of the interface in depth, i.e. its width (equivalent to the thickness of the lamella) is  $d$ . Taken from [19] (color figure online)

regions within the current path in the sample [67]. In all samples, where this noise was observed, it vanishes after applying a magnetic field of  $\sim 1$  kOe, a field that apparently influences the Josephson coupling between the superconducting regions. One expects interfaces where superconducting regions of different sizes exist at different positions within the interface. They can be Josephson coupled, in particular if the distance between those regions is small enough. We note further that Cooper pairs in a graphene layer have a large diffusion length of several hundreds of nm [69]. Therefore, it does seem possible to have Josephson coupled superconducting patches within the same interface.

The results of the lamella (c) with the Van der Pauw configuration of the electrodes shows a “negative” resistance at low temperature. This “negative” resistance is obtained from the negative voltage one measures in this Wheatstone-like bridge configuration, when one of the resistances tends to zero as described in detail in [67]. It is clear that an increase of the input current of two orders of magnitude changes qualitatively the temperature dependence of the evaluated resistance, see Fig. 7.20c. From this last result we may expect to have superconducting regions with critical



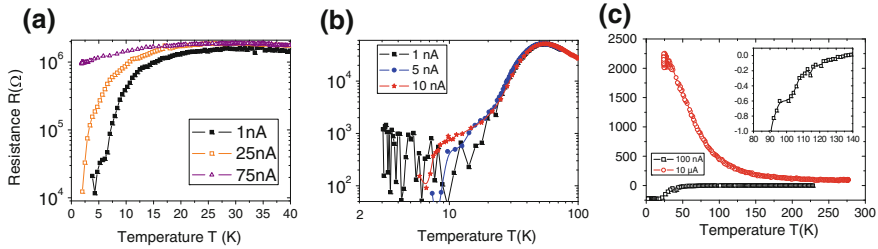


**Fig. 7.20** Resistance versus temperature at different input DC currents of three TEM lamellae with different sizes and different contact configurations. The resistance was calculated dividing the measured voltage (at the voltage electrodes) by the input current. The lamellae were prepared from HOPG samples of grade A. **a, b** Electrodes in linear configuration like the ones shown in Fig. 7.19; **c** electrodes in Van der Pauw configuration. The negative values of the resistance are due to this Van de Pauw configuration that provides negative voltages when one of the resistance in a Wheatstone-like bridge configuration tends to zero [67]. Adapted from [67, 68]

temperatures above 100 K, as the  $I-V$  characteristic curves suggest, see section (B) below.

The last point we would like to stress from the results shown in Fig. 7.20 is that the resistance does not go to zero at the lowest temperatures and lowest currents used in those measurements. There can be different reasons for this fact, like sensitivity of the instrument, noise level (whatever its origin) or a finite, non-superconducting resistance in the current path of the samples. A constant ohmic resistance in series would produce a finite slope in a  $I-V$  curve and its contribution might be easily subtracted. On the other hand we should note that a finite resistance, even below a critical Josephson current  $I_c$ , can appear due to thermally activated phase processes [70]. This thermally activation has to be taken into account to understand quantitatively the  $I-V$  measured curves.

### (B) Current-Voltage Characteristics

Figure 7.21 shows the  $I-V$  curves obtained at different temperatures for two lamellae [67] at no applied magnetic field. In the lamella with the Van der Pauw configuration, Fig. 7.21a, the curves show a non simple behavior upon temperature. With the assumption that the voltage measured can be understood in first approximation with a Wheatstone-like bridge configuration and that two of the resistors of the bridge have the influence of Josephson coupled superconducting regions, the curves can be well understood using the Josephson-coupling model with thermal activation [70]. Each of those resistors have a different effective Josephson critical current  $I_c(T)$ , the only free parameter in the model [67]. For the lamella with the contacts in series configuration, Fig. 7.21b, the curves can be also well fitted assuming only one effective Josephson critical current. We note that due to the thermally activation and upon the value of the Josephson critical current, the resistance does not strictly vanish at finite currents, even at 2 K. From the fits to those experimental curves, the temperature dependence of the Josephson critical current has been obtained for several lamellae

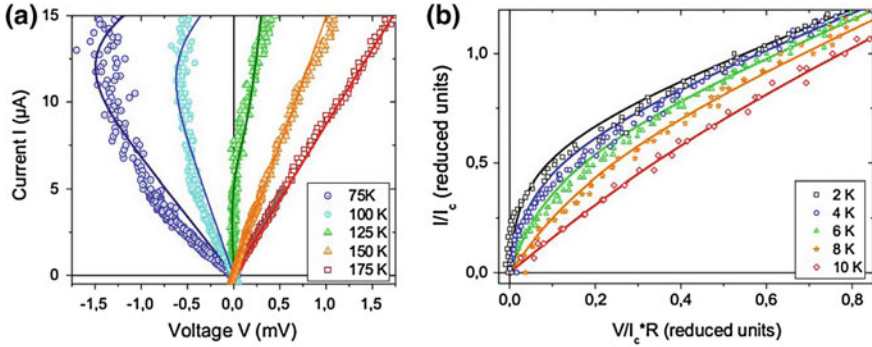


**Fig. 7.21** Current-voltage characteristic curves at different temperatures of two lamellae. **a** Lamella with a Van der Pauw contact configurations. The lines were calculated taking into account the Josephson-coupling model with thermal activation presented in [70] with two different Josephson critical currents  $I_c(T)$  from two resistors within a Wheatstone-like bridge configuration [67]. **b** Similar to (a) but in reduced units for a lamella with in series electrode configuration;  $R$  is the resistance at the critical temperature that is taken at high enough temperatures. The lines were calculated with the same model as in (a), but with only one Josephson critical current as free parameter;  $R$  is the resistance of the junction at the critical temperature, i.e. in the normal state, which in the case of the lamellae, it is usually taken directly from the measurement at a temperature where the apparent granular superconductivity behavior vanish. Adapted from [19, 68]

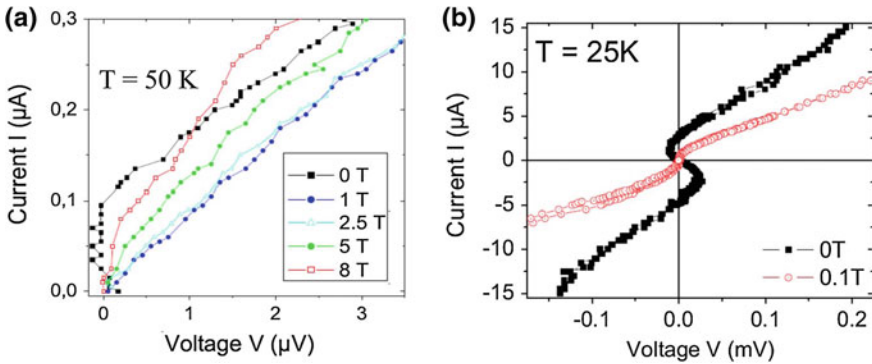


**Fig. 7.22** Current-voltage characteristic curves at different applied fields normal to the interfaces for two lamellae. **a** Lamella with usual contact configuration at a fixed temperature of 50 K and at different applied fields, adapted from [67]. **b** Characteristic curves obtained at 25 K for a lamella with Van der Pauw configuration at zero and 0.1 T applied fields. Adapted from [56]

[67] and it follows reasonably well the predictions for short junction length where the normal state barrier between the superconducting regions is a graphene layer [71].

### (C) Magnetic Field Dependence

The effect of an applied magnetic field to the transport behavior measured in the lamellae remains a puzzle and more experimental studies should be done in the near future. Figure 7.22 shows two results obtained in two lamellae of very different sizes

and with different contacts configurations. Figure 7.22a shows the  $I-V$  curves at 50 K of a rather thick ( $\sim 800$  nm) lamella. At zero field the  $I-V$  curve resembles the one of a Josephson junction. At a field of 1 T applied normal to the interfaces (and graphene layers) the resistance is finite at all measured currents and at larger field it starts to show a kind of reentrance at low enough currents. A field applied parallel to the interfaces does not affect the  $I-V$  curves within experimental error [67]. We note that a reentrance to a metallic-like state at low temperatures was observed in the longitudinal resistance of ordinary graphite bulk samples at high magnetic fields above that of the metal-insulator transition [72]. This kind of reentrance might be related to the one we observe in Fig. 7.22a. A kind of reentrance with magnetic field was also observed recently in an electric field-induced superconducting-like transition [73]. Its origin remains in all these cases unknown. Figure 7.22b shows the  $I-V$  curves of a lamella with contacts in the Van der Pauw configuration at a fixed temperature of 25 K and at zero and 0.1 T applied field. The  $s$ -like  $I-V$  curve can be quantitatively explained using a Wheatstone-bridge model and assuming that two resistors of the bridge follow the  $I-V$  Josephson characteristic with different critical Josephson currents, see also Fig. 7.21. A field of 0.1 T is enough to strongly affect the Josephson behavior especially in one of the resistors in the circuit.

An applied magnetic field is expected to be detrimental to the superconducting state. In the case of the granular superconductivity expected to occur within the interfaces and due to the Josephson like behavior, the magnetic field should affect also the Josephson coupling between the superconducting regions. Due to the expected Josephson array distribution within the interfaces and the unknown characteristics of the junctions it is not possible to predict a general behavior as a function of magnetic field. In fact, in some lamellae the applied field did not affect the characteristic curves within experimental error [67]. These results suggest that the effect of a magnetic field on the transport response of the interfaces might be size dependent, whereas the size can refer to the junction or to the superconducting regions.

At this stage we would like to note that superconductivity in single- as well as multiwall carbon nanotubes (CNT), was reported in more than 12 publications in the last 14 years [74–84]. The experimental data indicate that even individual double-wall CNT show superconductivity with critical temperatures from a few Kelvin to  $\sim 20$  K [82]. Superconductivity in 4 Å CNT is observed not in single but aligned and embedded in specially prepared matrices [80, 83]. Their behavior depends apparently on the coupling between each other along their length and through the matrix. The origin for the superconductivity in CNT in general is still a matter of discussion. If superconductivity exists in such a small pure carbon structure, we may speculate that a similar phenomenon should exist in certain regions of graphite. The observed field independence of the resistance in certain lamellae [67] resembles a similar field independence of the superconducting transition observed in CNT [80, 83] and interpreted as a sign of quasi 1D superconductivity, with thermally activated phase slips according to the Langer–Ambegaokar–McCumber–Halperin (LAMH) theory [85, 86]. This similarity suggests that upon the properties of the superconducting regions at certain interfaces in graphite samples, we may expect quasi 1D superconductivity, i.e. magnetic field independent broad resistivity transitions.

On the other hand the effects of a magnetic field on the superconducting state of 2D superconductors or in case the coupling does not correspond to a singlet state are not yet completely clarified. For example, superconductivity can be even enhanced by a parallel magnetic field to the interface where superconductivity is localized [87]. If the pairing is  $p$ -type [88] the influence of a magnetic field is expected to be qualitatively different from the conventional behavior [89, 90] with even an enhancement of the superconducting state at intermediate fields, in case the orbital diamagnetism can be neglected or for parallel field configuration. Further experimental studies are necessary to clarify the effect of a magnetic field to the state at the interfaces of lamellae of graphite samples of high grade.

### 7.3.1 Response of Lower Grade Samples

The response of lamellae obtained from HOPG samples of lower grade (i.e. larger rocking curve width) has been recently reported [7]. A TEM picture of the inner structure of this sample is shown in Fig. 7.2d. In that TEM picture it is clearly seen that the interfaces, i.e. the regions between different grey colors, are not as well defined as in the case of higher grade sample, i.e. compare it with the TEM picture of Fig. 7.2b. Therefore, if the interfaces are the reason for the behavior observed in the others lamella, we expect to measure clear differences in the electric response. Indeed, clear differences are observed in the temperature, current and field dependence. At high enough input currents ( $I \gtrsim 200$  nA) the electrical resistance of a lamella of this lower grade sample (SPI-II), increases decreasing temperature and tends to saturate at low temperatures [7]. A clear non-ohmic behavior is observed, namely the resistance decreases the larger the input current. In the low input current region ( $I < 200$  nA) the resistance starts to show a maximum at  $T \sim 3.5$  K, see Fig. 7.23a. With applied magnetic field this maximum vanishes. The curves shown in Fig. 7.23a follows qualitatively a similar MIT than the ones measure in usual bulk HOPG and kish graphite samples. A rough but similar scaling can be obtained from those curves that resembles the one obtained for higher grade HOPG samples [91]. There is, however, a difference that is worth to mention, namely the “critical” field  $H_c$ , necessary to trigger the transition from a metallic to an insulating state, is, roughly speaking, ten times larger in the lower grade sample than the  $H_c$  obtained in higher grade samples, i.e.  $\mu_0 H_c \sim 1$  T instead of  $\sim 0.1$  T [72, 92], see Fig. 7.23a. It is therefore tempting to relate this change to some specific characteristic of the internal interfaces. Assuming that the internal interfaces in both kind of samples have a similar range of twist angle and any possible doping within the interfaces is also similar, the main difference according to the TEM pictures would be related to the effective smaller size of well-defined 2D interface in the lower grade graphite samples, a conclusion compatible with the study done in [19] and discussed in Sect. 7.3.2.

The results shown in Fig. 7.23b, c, i.e. the non-linear  $I - V$  curves and the differential conductance  $G = dI/dV$  obtained from those curves, support further the existence of granular superconductivity in this kind of HOPG sample. Note that in

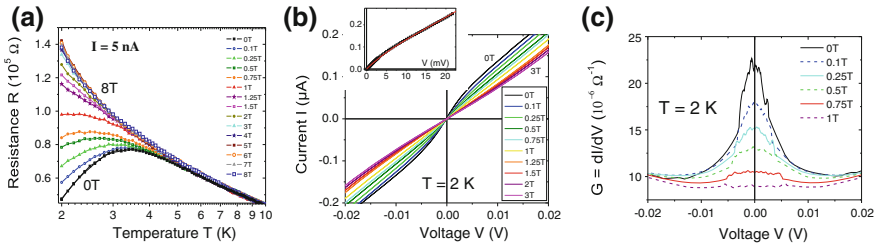


**Fig. 7.23** Results obtained of a lamella cut from a HOPG bulk sample grade B (SPI-II). **a** Resistance measured at a current of 5 nA versus temperature at different applied magnetic fields. **b**  $I-V$  curves at 2 K at different applied magnetic fields. The *inset* shows the result at zero field with the fit curve following [70] with a critical current of 82 nA. **c** Differential conductance calculated from the  $I-V$  curves at 2 K and at different applied fields. Adapted from [7]

the measured temperature range the resistance of the lamella does not reach a zero value at the used currents. The temperature dependence of the conductivity peak at zero voltage, (the curves are similar to those in Fig. 7.23c but at zero field at different fixed temperatures) follows an exponential temperature dependence [7], as observed in granular superconductors [31]. Extrapolating the conductance to zero temperature one concludes that most of the finite value at 2 K is due to thermal fluctuations [7]. In this case the  $I-V$  curves should follow a similar Josephson like dependence as observed in the other lamellae, see Fig. 7.21. The inset in Fig. 7.23b shows the  $I-V$  curve at 2 K at zero applied field and the fit following the equation derived in [70], calculated with an effective critical Josephson current of 82 nA [7].

### 7.3.2 Size Dependence

Most if not all the experimental facts indicate that the internal interfaces are the reason for the decrease of the resistance of graphite samples decreasing temperature. Several facts speak for the existence of granular superconductivity embedded in some of the interfaces. The questions arises regarding the dependence of the temperature at which the Josephson coupling between the expected superconducting regions starts to influence the measured voltage (or resistance). Comparing different graphite samples with interfaces, it appears that this “critical” temperature  $T_c$  depends much on the sample, whether it is a lamella or a bulk graphite or a graphite flake. However and in general, we observe that bulk samples of high order and with interfaces start to show this decrease in resistance at higher temperatures. This difference in  $T_c$  might be related to the size of the interface area, i.e. the smaller the area the lower is the temperature where the Josephson coupling starts to be effectively active. Certainly, this hypothesis is highly speculative because one does not know anything about the differences between intrinsic characteristics of the interfaces of different samples, like doping, twist angles, etc. Fig. 7.24 shows the temperature at which a maximum

is measured in the voltage-temperature curve of lamellae of different thickness  $d$ , this last defined in Fig. 7.19 [19]. The upper point represents the temperature of the maximum in the resistance for the bulk HOPG sample, from where the other lamellae were cut. The arrow indicates the expected range ( $1 \mu\text{m} \lesssim d \lesssim 10 \mu\text{m}$ ) for the size of the interfaces in the bulk sample, taking into account TEM [67] as well as EBSD [52] measurements.

The results in Fig. 7.24 suggest an apparent size dependence of this kind of “critical” temperature. That the real critical temperature  $T_c$  for superconductivity depends on the size of a sample, it is not completely unusual, although its origin is still under discussion and may depend on each case [93–95]. Taking into account that the observed behavior can be related to the existence of superconducting and normal conducting regions, one is allowed to compare those results with the the linear decrease of the superconducting critical temperature decreasing the *whole thickness* of an ensemble of superconducting/metal multilayers (leaving constant the thickness of each of the layers), see [93] and Refs. therein. The dashed-dotted straight line in Fig. 7.24 is the experimental line obtained for Nb/Al multilayers [93] multiplying by 10 both axes. We note that the obtained  $T_c(d)$  dependence of the lamellae has a nearly identical slope as that obtained for Nb/Al multilayers.

The origin for the change of  $T_c$  in conventional superconducting multilayers and thin wires has been tentatively given in [93, 94] based on weak localization (WL) corrections to  $T_c$  for 2D superconductors [95]. In both, the presence of disorder affects the screening of the Coulomb interaction resulting into an exponential suppression of  $T_c$ . As pointed out in [19], the parameter dependence of this exponential is different in the theory of [94] than the one used to fit the experimental results of Nb/Al multilayers in [93]. The continuous (green) line in Fig. 7.24 follows

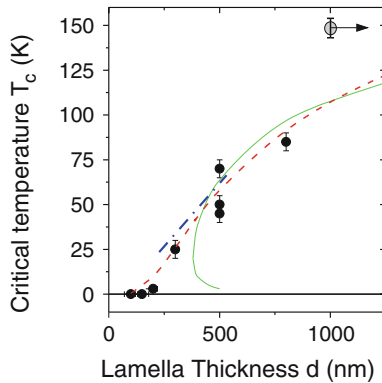


**Fig. 7.24** Critical temperature  $T_c$  versus thickness of the lamella. The critical temperature was taken at the maximum of the voltage versus temperature curve measured at 1 nA current, i.e. it is the temperature at which the Josephson coupling starts to affect the measured voltage. The thickness  $d$  of the lamella is defined in Fig. 7.19. For the meaning of the different curves see main text. Taken from [19]

$$T_c(d) = T_\infty e^{-\ell_{\text{th}}(T_c)/d}, \quad (7.2)$$

where  $T_\infty$  is the critical temperature for infinitely large samples,  $\ell_{\text{th}}(T) = (\hbar D/k_B T)^{1/2}$  is the thermal length at temperature  $T$ ,  $D = v_F \ell/2$  the 2D diffusion constant, with  $v_F \approx 10^6$  m/s the Fermi velocity and  $\ell$  the mean free path. Independent measurements done in graphite flakes without (or with much less influence of) interfaces provide  $\ell \sim 3 \mu\text{m}$  at  $T < 100$  K [34] and therefore  $D \sim 1.5 \times 10^4$  cm<sup>2</sup>/s, a value four orders of magnitude larger than the one used in [93], meaning that the effect is relevant in far thicker samples or at much higher temperatures than in Nb/Al multilayers with  $T_c \lesssim 10$  K. With this diffusion constant and  $T_\infty = 150$  K the obtained numerical solution of (7.2) is the continuous green line in Fig. 7.24. The semiquantitative agreement is remarkable as well as the estimated cut-off  $d_{\text{min}} = \ell_{\text{th}}(T_c)/2.7 \approx 0.38 \mu\text{m}$ , below which (7.2) has no solution.

Following [19], the important aspect of the disorder correction in [94] is screening and the parameter controlling the correction is  $t = (e^2/(2\pi^2\hbar))R_\square$ , where  $R_\square$  is the sheet resistance [94]. In the limit  $t \ll \gamma^2$ , where  $\gamma$  is the dimensionless bare BCS coupling parameter, the effective critical temperature is

$$T_c(d) = T_\infty \exp^{-t(d)/(6\gamma^3)} = T_\infty \exp^{-\alpha/d}, \quad (7.3)$$

where  $\alpha = t(d)/(6\gamma^3)$ . The dashed line in Fig. 7.24 shows a fit of this type of behavior to the data of [19]. A discussion of the validity range of the approach in [94] and of the parameters obtained from the fits can be read in [19].

## 7.4 Conclusion

There are clear experimental and theoretical evidence on the existence of specific electronic properties, such as the enhanced density of states in multilayer graphene, twisted graphene as well as at the grain boundaries of graphene or graphite. These electronic peculiarities coming from these defects or interfaces will undoubtedly affect the electronic transport properties measured in graphite and determine the metallic and/or superconducting behavior of whole samples. The existence of rhombohedral stacking order regions embedded in an overall Bernal stacking order matrix and/or twisted Bernal ordered regions may provide a key contribution to understand several details of the transport properties of graphite samples. Taking these peculiarities into account, it is not necessary to speculate too much to arrive to the conclusion that transport and magnetization measurements may change upon microstructure of the graphite sample in question. These differences between samples or changes after certain treatment of a given sample remain difficult to predict and understand if we do not know the internal interface structure and further characteristics. For example, in [96] evidence has been obtained for the change in the structure of AB and BA domains in bilayer graphene after annealing at 1,000 to 1,200 °C.

The interfaces observed in bulk graphite exist also in graphite powders before as well as after certain treatments and may well be the reason for the superconducting-like response measured in magnetization and transport measurements [5, 7, 67, 97]. It should be also clear that if the interfaces play a main role in the measured properties, then time dependence, instabilities or even the apparent irreproducibility of some of the obtained results can be expected, unless one is able to fix the properties and density of the interfaces in a given sample. The existence of high-temperature superconductivity in (non-intercalated) graphite, even with critical temperatures above room-temperature, has been claimed in different publications of the last 40 years [98–104]. These independent reports show some striking peculiarities: The superconducting signal shows low reproducibility, some signals are not stable in time, the amount of superconducting mass (if at all) is small and there is no clear idea on the superconducting phase(s). These peculiarities and the general (over)skepticism in the community on the reported evidence are the reasons, why there was so little interest in this kind of phenomenon. If we assume that interfaces are the reason for all these signals, the interest of the community on these tantalizing phenomena should improve in the future.

We gratefully acknowledge Tero Heikkilä and Grigori Volovik for the fruitful discussions. Y.V.L. acknowledges the support given by the Russian Government Program of Competitive Growth of Kazan Federal University.

## References

1. M.S. Dresselhaus, G. Dresselhaus, K. Sugihara, I.L. Spain, H.A. Goldberg, *Graphite Fibers and Filaments* (Springer, Berlin, 1988)
2. R.H. Telling, M.I. Heggie, *Philos. Mag.* **87**, 4797 (2007)
3. M. Inagaki, *New Carbons: Control of Structure and Functions* (Elsevier, New York, 2000)
4. J. Barzola-Quiquia, J.L. Yao, P. Rödiger, K. Schindler, P. Esquinazi, *Phys. Status Solidi (a)* **205**, 2924 (2008)
5. T. Scheike, W. Böhlmann, P. Esquinazi, J. Barzola-Quiquia, A. Ballestar, A. Setzer, *Adv. Mater.* **24**, 5826 (2012)
6. P. Esquinazi, T.T. Heikkilä, Y.V. Lysogorskiy, D.A. Tayurskii, G.E. Volovik, *JETP Lett.* **100**, 336 (2014). [arXiv:1407.1060](https://arxiv.org/abs/1407.1060)
7. A. Ballestar, P. Esquinazi, W. Böhlmann, *Phys. Rev. B* **91**, 014502 (2015)
8. M. Kuwabara, D.R. Clarke, A.A. Smith, *Appl. Phys. Lett.* **56**, 2396 (1990)
9. M. Flores, E. Cisternas, J. Correa, P. Vargas, *Chem. Phys.* **423**, 49 (2013)
10. L. Feng, X. Lin, L. Meng, J.C. Nie, J. Ni, L. He, *Appl. Phys. Lett.* **101**, 113113 (2012)
11. D. Tománek, S.G. Louie, *Phys. Rev. B* **37**, 8327 (1988)
12. J.M. Campanera, G. Savini, I. Suarez-Martinez, M.I. Heggie, *Phys. Rev. B* **75**, 235449 (2007)
13. D.L. Miller, K.D. Kubista, G.M. Rutter, M. Ruan, W.A. de Heer, P.N. First, J.A. Stroscio, *Phys. Rev. B* **81**, 125427 (2010)
14. Y. Zhang, J.P. Small, W.V. Pontius, P. Kim, *Appl. Phys. Lett.* **86**, 073104 (2005)
15. Y. Lu, M. Muñoz, C.S. Steplecaru, C. Hao, M. Bai, N. García, K. Schindler, P. Esquinazi, *Phys. Rev. Lett.* **97**, 076805 (2006). See also the comment by S. Sadewasser, Th. Glatzel, *Phys. Rev. Lett.* **98**, 269701 (2007) and the reply by Lu et al., *idem* **98**, 269702 (2007) and also R. Proksch, *Appl. Phys. Lett.* **89**, 113121 (2006)



16. I. Brihuega, P. Mallet, H. González-Herrero, G.T. de Laissardière, M.M. Ugeda, L. Magaud, J.M. Gómez-Rodríguez, F. Ynduráin, J.Y. Veullen, *Phys. Rev. Lett.* **109**, 196802 (2012)
17. P. San-Jose, E. Prada, *Phys. Rev. B* **88**, 121408(R) (2013)
18. H. Ribeiro, K. Sato, G. Eliel, E. de Souza, C.C. Lu, P.W. Chiu, R. Saito, M. Pimenta, *Carbon* **90**, 138 (2015)
19. A. Ballestar, T.T. Heikkilä, P. Esquinazi, *Superc. Sci. Technol.* **27**, 115014 (2014)
20. J. Lahiri, Y. Lin, P. Bozkurt, I. Oleynik, M. Batzill, *Nat. Nanotechnol.* **5**, 326 (2010)
21. P. Esquinazi, A. Setzer, R. Höhne, C. Semmelhack, Y. Kopelevich, D. Spemann, T. Butz, B. Kohlstrunk, M. Lösche, *Phys. Rev. B* **66**, 024429 (2002)
22. N.B. Kopnin, M. Ijäs, A. Harju, T.T. Heikkilä, *Phys. Rev. B* **87**, 140503 (2013)
23. W.A. Muñoz, L. Covaci, F. Peeters, *Phys. Rev. B* **87**, 134509 (2013)
24. B.T. Kelly, *Physics of Graphite* (Applied Science Publishers, London, 1981)
25. Q. Lin, T. Li, Z. Liu, Y. Song, L. He, Z. Hu, Q. Guo, H. Ye, *Carbon* **50**, 2369 (2012)
26. S. Hattendorf, A. Georgi, M. Liebmann, M. Morgenstern, *Surf. Sci.* **610**, 53 (2013)
27. D. Pierucci, H. Sediri, M. Hajlaoui, J.C. Girard, T. Brumme, M. Calandra, E. Velez-Fort, G. Patriarche, M.G. Silly, G. Ferro, V. Soulière, M. Marangolo, F. Sirotti, F. Mauri, A. Ouerghi, *ACS Nano* **9**, 5432 (2015)
28. Y. Henni, H.P. Ojeda Collado, K. Nogajewski, M.R. Molas, G. Usaj, C.A. Balseiro, M. Orlita, M. Potemski, C. Faugeras, [arXiv:1603.03611](https://arxiv.org/abs/1603.03611)
29. M. Zoraghi, J. Barzola-Quiquia, M. Stiller, A. Setzer, P. Esquinazi, G.H. Kloeß, T. Muenster, T. Lühmann, I. Estrela-Lopis, [arXiv:1603.06365](https://arxiv.org/abs/1603.06365)
30. N. García, P. Esquinazi, J. Barzola-Quiquia, S. Dusari, *New J. Phys.* **14**(5), 053015 (2012)
31. Y. Shapira, G. Deutscher, *Phys. Rev. B* **27**, 4463 (1983)
32. P. Esquinazi, N. García, J. Barzola-Quiquia, P. Rödiger, K. Schindler, J.L. Yao, M. Ziese, *Phys. Rev. B* **78**, 134516 (2008)
33. N. García, P. Esquinazi, J. Barzola-Quiquia, B. Ming, D. Spoddig, *Phys. Rev. B* **78**, 035413 (2008)
34. P. Esquinazi, J. Barzola-Quiquia, S. Dusari, N. García, *J. Appl. Phys.* **111**, 033709 (2012)
35. Y. Ohashi, T. Hironaka, T. Kubo, K. Shiiki, *TANSO* **195**, 410 (2000)
36. Y. Ohashi, K. Yamamoto, T. Kubo, *Carbon'01, An International Conference on Carbon*, Lexington, KY, United States, 14–19 July. (The American Carbon Society, 2001), pp. 568–570. [www.acs.omnibooksonline.com](http://www.acs.omnibooksonline.com)
37. K. Thiyagarajan, B. Saravanakumar, R. Mohan, S.J. Kim, *Sci. Adv. Mater.* **5**, 542 (2013)
38. J. Barzola-Quiquia, S. Dusari, G. Bridoux, F. Bern, A. Molle, P. Esquinazi, *Nanotechnology* **21**, 145306 (2010)
39. I.A. Luk'yanchuk, Y. Kopelevich, *Phys. Rev. Lett.* **93**, 166402 (2004)
40. R. Ruffieux, O. Gröning, P. Schwaller, L. Schlapbach, P. Gröning, *Phys. Rev. Lett.* **84**, 4910 (2000)
41. A. Arndt, D. Spoddig, P. Esquinazi, J. Barzola-Quiquia, S. Dusari, T. Butz, *Phys. Rev. B* **80**, 195402 (2009)
42. V.T. Dolgoplov, A.A. Shashkin, G.V. Kravchenko, I.M. Mukhametzhano, M. Wendel, J.P. Kotthaus, L.W. Molenkamp, C.T. Foxon, *JETP Lett.* **63**, 63 (1996)
43. N. Harrison, J. Singleton, *J. Phys.: Condens. Matter* **13**, L463 (2001)
44. P. Esquinazi, J. Krüger, J. Barzola-Quiquia, R. Schönemann, T. Hermannsdörfer, N. García, *AIP Adv.* **4**, 117121 (2014)
45. X. Du, I. Skachko, A. Barker, E.Y. Andrei, *Nat. Nanotechnol.* **3**, 491 (2008)
46. S. Dusari, J. Barzola-Quiquia, P. Esquinazi, N. García, *Phys. Rev. B* **83**, 125402 (2011)
47. N. García, L. Escapa, *Appl. Phys. Lett.* **54**, 1418 (1989)
48. I. Snyman, J. Tworzydło, C.W.J. Beenakker, *Phys. Rev. B* **78**, 045118 (2008)
49. J.L. Costa-Krämer, N. García, H. Olin, *Phys. Rev. Lett.* **78**, 4990 (1997)
50. B.J. van Wees, H. van Houten, C.W.J. Beenakker, J.G. Williamson, L.P. Kouwenhoven, D. van der Marel, C.T. Foxon, *Phys. Rev. Lett.* **60**, 848 (1988)
51. D.A. Wharam, T.J. Thornton, R. Newbury, M. Pepper, H. Ahmed, J.E.F. Frost, D.G. Hasko, D.C. Peacock, D.A. Ritchie, G.A.C. Jones, *J. Phys. C: Solid State Phys.* **21**, L209 (1988)

52. J.C. González, M. Muñoz, N. García, J. Barzola-Quiquia, D. Spoddig, K. Schindler, P. Esquinazi, *Phys. Rev. Lett.* **99**, 216601 (2007)
53. J.W. McClure, *IBM J. Res. Dev.* **8**, 255 (1964)
54. A. Grüneis, C. Attacalite, T. Pichler, V. Zabolotnyy, H. Shiozawa, S.L. Molodtsov, D. Inosov, A. Koitzsch, M. Knupfer, J. Schiessling, R. Follath, R. Weber, P. Rudolf, R. Wirtz, A. Rubio, *Phys. Rev. Lett.* **100**, 037601 (2008)
55. A. Kumar, J.M. Poumirol, W. Escoffier, M. Goiran, B. Raquet, J.C. Pivin, *J. Phys.: Condens. Matter* **22**, 436004 (2010)
56. J. Barzola-Quiquia, A. Ballestar, S. Dusari, P. Esquinazi, *Experimental Study of the Intrinsic and Extrinsic Transport Properties of Graphite and Multigraphene Samples* (Intech, Open Access Publisher, Jian Ru Gong (ed.), 2011), chap. 8. ISBN 978-953-307-292-0
57. F. Hund, B. Mrowka, *Sächs. Akad. Wiss., Leipzig* **87**, 185 (1935)
58. G.E. Kimball, *J. Chem. Phys.* **3**, 560 (1935)
59. F. Hund, B. Mrowka, *Sächs. Akad. Wiss., Leipzig* **87**, 325 (1935)
60. P.R. Wallace, *Phys. Rev.* **71**, 622 (1947)
61. R.O. Dillon, I.L. Spain, J.W. McClure, *J. Phys. Chem. Solids* **38**, 635 (1977)
62. J.M. Schneider, M. Orlita, M. Potemski, D.K. Maude, *Phys. Rev. Lett.* **102**, 166403 (2009). see also the comment by I.A. Luk'yanchuk, Y. Kopelevich, *idem* **104**, 119701 (2010)
63. I.M. Tsidilkovski, *Electron Spectrum of Gapless Semiconductors*, vol. 116, Springer Series in Solid-State Sciences (Springer, New York, 1997)
64. T. Stauber, N.M.R. Peres, F. Guinea, *Phys. Rev. B* **76**, 205423 (2007)
65. J. Barzola-Quiquia, P. Esquinazi, *J. Supercond. Nov. Magn.* **23**, 451 (2010)
66. H. Kempa, H.C. Semmelhack, P. Esquinazi, Y. Kopelevich, *Solid State Commun.* **125**, 1 (2003)
67. A. Ballestar, J. Barzola-Quiquia, T. Scheike, P. Esquinazi, *New J. Phys.* **15**, 023024 (2013)
68. Ana Ballestar, Ph.D. thesis entitled "Superconductivity at graphite interfaces", University of Leipzig (2014), unpublished
69. H.B. Heersche, P. Jarillo-Herrero, J.B. Oostinga, L.M.K. Vandersypen, A.F. Morpurgo, *Nature* **446**, 56 (2007)
70. V. Ambegaokar, B.I. Halperin, *Phys. Rev. Lett.* **22**, 1364 (1969)
71. I. Hagymási, A. Kormányos, J. Cserti, *Phys. Rev. B* **82**, 134516 (2010)
72. Y. Kopelevich, J.H.S. Torres, R.R. da Silva, F. Mrowka, H. Kempa, P. Esquinazi, *Phys. Rev. Lett.* **90**, 156402 (2003)
73. A. Ballestar, P. Esquinazi, J. Barzola-Quiquia, S. Dusari, F. Bern, R. da Silva, Y. Kopelevich, *Carbon* **72**, 312 (2014)
74. Z.K. Tang, L. Zhang, N. Wang, X.X. Zhang, G.H. Wen, G.D. Li, J.N. Wang, C.T. Chan, P. Sheng, *Science* **292**, 2462 (2001)
75. M. Kociak, A.Y. Kasumov, S. Guéron, B. Reulet, I.I. Khodos, Y.B. Gorbatov, V.T. Volkov, L. Vaccarini, H. Bouchiat, *Phys. Rev. Lett.* **86**, 2416 (2001)
76. M. Ferrier, F. Ladieu, M. Ocio, B. Sacépé, T. Vaugien, V. Pichot, P. Launois, H. Bouchiat, *Phys. Rev. B* **73**, 094520 (2006)
77. I. Takesue, J. Haruyama, N. Kobayashi, S. Chiashi, S. Maruyama, T. Sugai, H. Shinohara, *Phys. Rev. Lett.* **96**, 057001 (2006)
78. N. Murata, J. Haruyama, Y. Ueda, M. Matsudaira, H. Karino, Y. Yagi, E. Einarsson, S. Chiashi, S. Maruyama, T. Sugai, N. Kishi, H. Shinohara, *Phys. Rev. B* **76**, 245424 (2007)
79. T. Tsuneta, L. Lechner, P.J. Hakonen, *Phys. Rev. Lett.* **98**, 087002 (2007)
80. R. Lortz, Q. Zhang, W. Shi, J.T. Ye, C. Qiu, Z. Wang, H. He, P. Sheng, T. Qian, Z. Tang, N. Wang, X. Zhang, J. Wang, C.T. Chan, *Proc. Natl. Acad. Sci.* **106**(18), 7299 (2009)
81. Z. Wang, W. Shi, H. Xie, T. Zhang, N. Wang, Z. Tang, X. Zhang, R. Lortz, P. Sheng, I. Sheikin, A. Demuer, *Phys. Rev. B* **81**, 174530 (2010)
82. W. Shi, Z. Wang, Q. Zhang, Y. Zheng, C. Jeong, M. He, R. Lortz, Y. Cai, N. Wang, T. Zhang, H. Zhang, Z. Tang, P. Sheng, H. Muramatsu, Y.A. Kim, M. Endo, P.T. Araujo, M.S. Dresselhaus, *Sci. Rep.* **2**, 625 (2012)
83. Z. Wang, W. Shi, R. Lortz, P. Sheng, *Nanoscale* **4**, 21 (2012)

84. J. Barzola-Quiquia, P. Esquinazi, M. Lindel, D. Spemann, M. Muallem, G. Nessim, *Carbon* **88**, 16 (2015)
85. J.S. Langer, V. Ambegaokar, *Phys. Rev.* **164**, 498 (1967)
86. D.E. McCumber, B.I. Halperin, *Phys. Rev. B* **1**, 1054 (1970)
87. H.J. Gardner, A. Kumar, L. Yu, P. Xiong, M.P. Warusawithana, L. Wang, O. Vafek, D.G. Schlom, *Nat. Phys.* **7**, 895 (2011)
88. J. González, F. Guinea, M.A.H. Vozmediano, *Phys. Rev. B* **63**, 134421 (2001)
89. K. Scharnberg, R.A. Klemm, *Phys. Rev. B* **22**, 5233 (1980)
90. A. Knigavko, B. Rosenstein, *Phys. Rev. B* **58**, 9354 (1998)
91. Y. Kopelevich, P. Esquinazi, J.H.S. Torres, R.R. da Silva, H. Kempa, Graphite as a highly correlated electron liquid, in *Advances in Solid State Physics*, vol. 43, ed. by B. Kramer (Springer, Berlin, 2003), pp. 207–222
92. H. Kempa, Y. Kopelevich, F. Mrowka, A. Setzer, J.H.S. Torres, R. Höhne, P. Esquinazi, *Solid State Commun.* **115**, 539 (2000)
93. J. Guimpel, M.E. de la Cruz, F. de la Cruz, H.J. Fink, O. Laborde, J.C. Villegier, *J. Low Temp. Phys.* **63**, 151 (1986)
94. Y. Oreg, A. Finkel'stein, *Phys. Rev. Lett.* **83**, 191 (1999)
95. H. Fukuyama, *Physica* **126B**, 306 (1984). See also H. Ebisawa, H. Fukuyama, S. Maekawa, *J. Phys. Soc. Jpn.* **54**, 2257 (1985)
96. J.S. Alden, A.W. Tsen, P.Y. Huang, R. Hovden, L. Brown, J. Park, D.A. Muller, P.L. McEuen, *Proc. Natl. Acad. Sci.* **110**, 11256 (2013)
97. T. Scheike, P. Esquinazi, A. Setzer, W. Böhlmann, *Carbon* **59**, 140 (2013)
98. K. Antonowicz, *Nature* **247**, 358 (1974)
99. R.R. da Silva, J.H.S. Torres, Y. Kopelevich, *Phys. Rev. Lett.* **87**, 147001 (2001)
100. H.P. Yang, H.H. Wen, Z.W. Zhao, S.L. Li, *Chin. Phys. Lett.* **18**, 1648 (2001)
101. S. Moehlecke, P.C. Ho, M.B. Maple, *Philos. Mag. B* **82**, 1335 (2002)
102. I. Felner, Y. Kopelevich, *Phys. Rev. B* **79**, 233409 (2009)
103. S.W. Han, J.D. Lee, J.P. Noh, D.W. Jung, *J. Low Temp. Phys.* **160**, 41 (2010)
104. Y. Kawashima, *AIP Adv.* **3**, 052132 (2013)